JCTC Journal of Chemical Theory and Computation

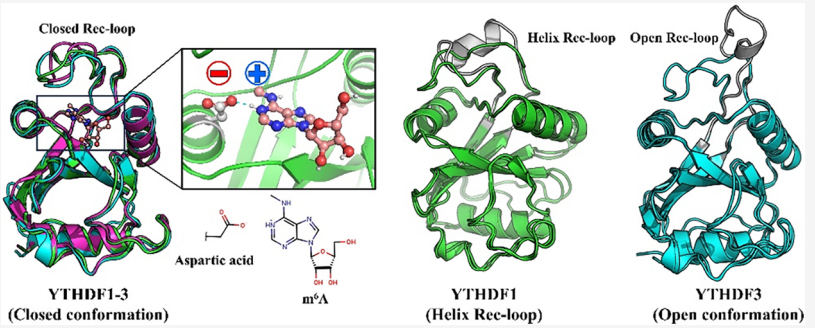
pubs.acs.org/JCTC Article

Recognition Loop Dynamics Differentiates m^{6}A-mRNA Reader Domains of YTHDF Proteins

Yaozong Li,[‖] Rajiv Kumar Bedi,[‖] Pedro Ojeda-May, and Amedeo Caflisch*

Cite This: https://doi.org/10.1021/acs.jctc.6c01247 Read Online

ACCESS | Metrics & More | Article Recommendations | Supporting Information



ABSTRACT: The three human YTH-domain family proteins (YTHDF1, YTHDF2, and YTHDF3) are highly homologous and recognize the N^6-methyladenosine (m^{6}A) modification of mRNA with essentially identical binding modes and affinities. This homogeneity challenges the well-established view that different YTHDF proteins play distinct cellular functions (the specificity view), with an emerging argument that these proteins may instead play redundant roles. To study this apparent discrepancy, we investigated the mechanism of binding of m^{6}A-containing RNA using mutagenesis, X-ray crystallography, isothermal titration calorimetry (ITC), and molecular dynamics simulations. Specifically, we compared different properties of YTHDF proteins, including their binding capacities to m^{6}A-RNA, conformational changes, and homodimerization propensity. Our results show that the YTHDF proteins share an identical binding mode of m^{6}A-RNA, which requires rare protonation of m^{6}A for binding. Additionally, the three proteins share a similar open-closed switch for their recognition loop regulating the m^{6}A binding. On the other hand, ITC data and crystal structures provide consistent evidence that the YTHDF proteins differ significantly in the flexibility of the recognition loop and its conformational preferences. Only YTHDF1 can homodimerize, which prevents binding to m^{6}A-RNA. Furthermore, we integrate the available biophysical and biochemical evidence to define both the shared and distinct features of YTHDF1−3 in m^{6}A-RNA recognition and propose a hybrid model that reconciles the redundancy-specificity debate. Finally, we discuss the limitations of the work and propose experiments for validating the presented model.

INTRODUCTION

Recent studies have uncovered new information about modifications in RNA, leading to the emergence of a new field known as RNA epigenetics,[1] or epitranscriptomics.[2] The prominent N^6-methyladenosine (m^{6}A) modification is crucial in controlling various biological functions of mRNA (mRNA). Adding and removing m^{6}A are reversible and dynamic processes regulated by writer and eraser proteins.[3] The protein complex METTL3/METTL14[4] adds the m^{6}A modification to mRNA, whereas eraser proteins like FTO[5] and ALKBH5[6] can remove it. Reader proteins, including YTHDC1,[7] YTHDC2,[8] YTHDF1−3,[7,9] and IGF2BPs,[10] bind to the methylated RNA, thereby controlling cellular functions. YTHDF1−3 are primarily found in the cytoplasm of mammalian cells and regulate mRNA metabolism.

Experimental studies have revealed distinct roles for YTHDF1−3 (abbreviated in the following as DF1−3). DF1 enhances translation by interacting with ribosomes and translation-initiating factors.[11] DF2 promotes the degradation of m^{6}A-marked mRNA by recruiting the RNA decay machinery.[12] DF3 assists in regulating mRNA fate through interactions with DF1 and DF2.[13] However, recent findings suggest that these proteins may have overlapping functions.[14] This unified model is supported by their high similarity in sequence (86% identity in the YTH domain, Figure S1), structure,[15−17] and dynamics.[16] Furthermore, all three YTHDF proteins exhibit similar binding affinity to m^{6}A-RNAs in various assays.[14,18] They can also promote liquid−liquid phase

Received: June 20, 2026
Revised: October 1, 2026
Accepted: October 5, 2026

ACS Publications © XXXX American Chemical Society

https://doi.org/10.1021/acs.jctc.6c01247
J. Chem. Theory Comput. XXXX, XXX, XXX−XXX

Downloaded from pubs.acs.org/jctcce/article-pdf/doi/10.1021/acs.jctc.6c01247/6884938/acs.jctc.6c01247.pdf by UNIV OF ZURICH user on 20 October 2026

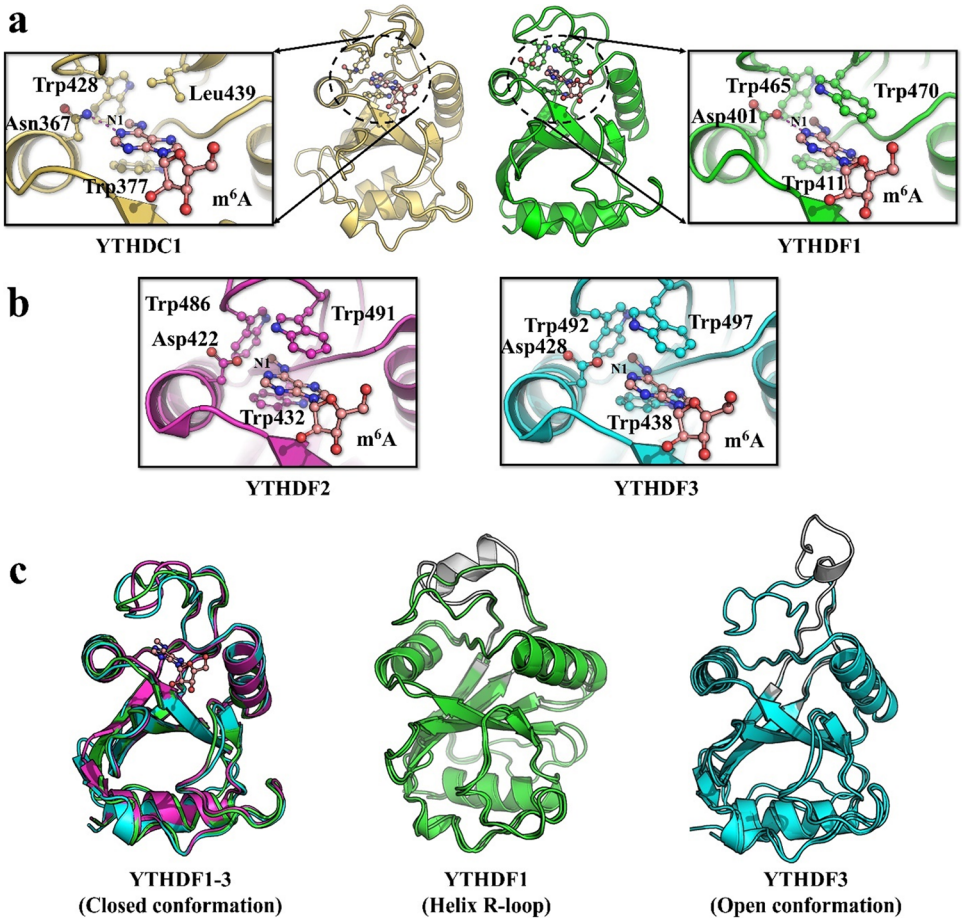


Figure 1. YTH domains of m^{6}A reader proteins. (a) Comparison of YTHDC1 and DF1 interacting with m^{6}A. (b) Interaction details of DF2 and DF3 to m^{6}A. (c) Different crystallized conformations of DF1−3. The closed conformations were generated from the crystal structures of holo DF1 (PDB code 4RCJ, colored in green), DF2 (PDB code 7Z26, pink), and DF3 (PDB code 6ZOT, cyan). Their open conformations (gray, PDB codes 8BS4 and 8BS5 for DF1 and DF3, respectively) are structurally overlapped in the regular elements of secondary structure.

separation,[19−21] enabling them to merge into processing bodies or organelles.

DF1−3 proteins play diverse roles in different types of cancers,[22−29] where upregulated DF1 enhances the translation of oncogenes, while overexpressed DF2 promotes the degradation of oncogene suppressors. Depending on the tumor types, DF3 may have opposing functions by stabilizing or destabilizing related mRNAs. In most cases, DF1−3 acts as an oncogene, suggesting its potential as a therapeutic target for treating cancer. However, the structural basis for these unique functions of DF1−3 remains to be determined. A recent study attributes the differences to their low-complexity regions rather than to YTH domains.[30]

In this study, we employ a multidisciplinary approach consisting of mutagenesis, X-ray crystallography, isothermal titration calorimetry (ITC), and molecular dynamics (MD) simulations to shed light on the similarities and differences among DF1−3. The *in vitro* experiments and *in silico* studies focused on their YTH domains reveal that, despite the highly similar YTH domains, DF1 exhibits higher flexibility of the m^{6}A recognition loop (Rec-loop). We discuss the implications of our findings for cellular functions and the redundancy-specificity debate. Additionally, we propose potential applications of the new crystal structures and biochemical tools for the design of selective inhibitors.[15,31−34]

RESULTS

Protonation of m^{6}A for Binding to the Asp Side Chain in the Cage of the YTHDF Domains

The three DF proteins, DC1, and DC2 recognize m^{6}A specifically through their aromatic cages and five hydrogen bonds.[32,34−36] While N1 of m^{6}A is involved in a favorable hydrogen bond with the side chain of Asn367 of DC1, it also apparently forms a polar contact with an aspartate in the aromatic cage of DF1−3 (Figure 1a,b). For instance, the crystal structure of DF1 (PDB code 4RCJ) shows a 2.7 Å distance between a carboxyl oxygen atom of Asp401 and N1 of m^{6}A.[17] However, it is unclear whether the proton associates with Asp401 or m^{6}A. The pK_a values of both chemical entities are similar in aqueous solution (approximately 3.6).[37]

To determine whether m^{6}A-RNA recognition is pH-dependent, we measured the binding of GG(m^{6}A)CU to DF1 by ITC under acidic (pH 5.0) and near-physiological (pH 7.4) conditions. Direct comparison of wild-type DF1 at the two pH values was complicated by its pH-dependent homodimerization, which is characterized in detail in a later section. Briefly, DF1 remains predominantly monomeric at pH 5.0, allowing direct measurement of RNA binding, whereas at pH 7.4, homodimerization partially occludes the m^{6}A-RNA-binding site. We therefore introduced the R542A mutation to disrupt dimerization and assess RNA binding at pH 7.4 with

Downloaded from pubs.acs.org/jctce/article-pdf/doi/10.1021/acs.jctc.6c01247/6884938/acs.jctc.6c01247.pdf by UNIV OF ZURICH user on 20 October 2026

https://doi.org/10.1021/acs.jctc.6c01247
J. Chem. Theory Comput. XXXX, XXX, XXX−XXX

Table 1. Isothermal Titration Calorimetry (ITC) Data of DF1-3 Binding to GG(m^{6}A)CU at pH = 5[a,b,c]

	N	ΔH (kcal/mol)	ΔS (cal/mol/deg)	$-T\Delta S$ (kcal/mol)	K_d (μM)	ΔG (kcal/mol)
(wt)DF1	1.02 ± 0.016	−16.4 ± 0.36	−27.2	8.1 ± 0.4	0.8	−8.3 ± 0.15
(ds)DF1	1.02 ± 0.015	−15.3 ± 0.32	−23.6	7.0 ± 0.34	0.9	−8.2 ± 0.12
(wt)DF2	1.04 ± 0.018	−13.2 ± 0.34	−16.1	4.8 ± 0.4	0.6	−8.4 ± 0.2
(ds)DF2	1 (fixed)				27.7	−6.2
(wt)DF3	1.11 ± 0.01	−12.9 ± 0.13	−15.2	4.5 ± 0.15	0.8	−8.3 ± 0.07
(ds)DF3	1.09 ± 0.01	−11.1 ± 0.12	−12.3	3.7 ± 0.13	3.7	−7.4 ± 0.04

[a]wt: wild type. [b]ds: disulfide-bonded mutant. DF1, Ser398Cys and Ser466Cys; DF2, Ser419Cys and Ser487Cys; DF3, Ser425Cys and Ser493Cys. [c]The standard errors were derived from fitting of the ITC titration curves.

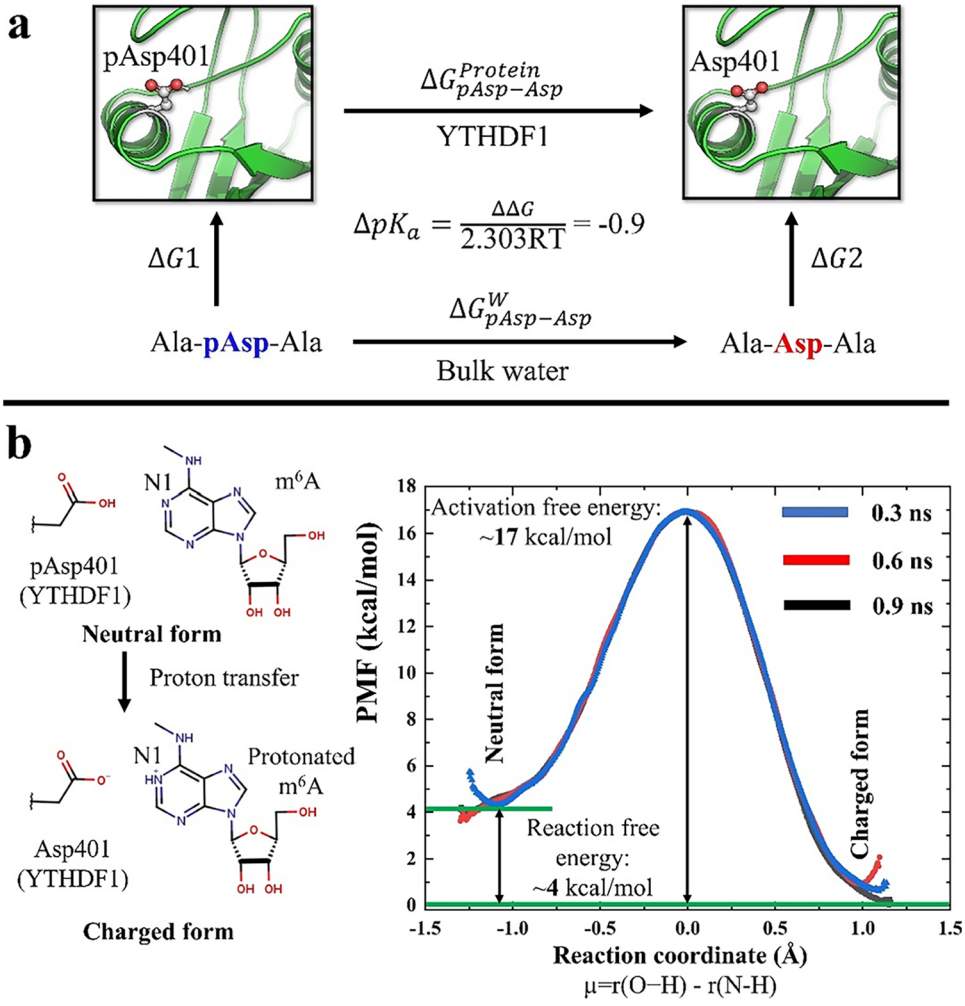


Figure 2. Unique hydrogen bonding of DF1 m^{6}A. (a) Thermodynamic cycle of FEP simulations for calculating the shift in pK_a between a model Asp-containing tripeptide and the Asp401 side chain in the apo state of DF1. (b) Free energy profiles of proton shuttling between DF1 and m^{6}A. The profiles were obtained via semiempirical QM/MM simulations. The profiles are essentially identical irrespective of the sampling time (colors in the legend), which provides evidence of convergence. The 2D chemical structures were drawn by MarvinSchetch.[39]

minimal interference from the dimeric state. Wild-type DF1 bound GG(m^{6}A)CU with a K_d of 0.8 μM at pH 5.0, whereas no detectable binding was observed for wild-type DF1 at pH 7.4. In contrast, the R542A mutant retained measurable binding at pH 7.4, with a K_d of approximately 108 μM (Tables 1 and S1). The approximately 135-fold difference in binding affinity indicates a pronounced pH dependence of m^{6}A-RNA recognition and is consistent with enhanced polar interactions at lower pH arising from a shift in the protonation equilibrium of Asp401 and/or m^{6}A.

To determine the binding mechanism at an atomic level of detail, we examined the possibility of locating the proton on Asp401 of DF1 in its closed apo form by conducting free energy perturbation (FEP) calculations (Figure 2a). Surprisingly, Asp401 in the aromatic cage is deprotonated with an even higher chance than that of a model Ala-Asp-Ala peptide in bulk water according to the calculated pK_a value (i.e., a shift of −0.9 pK_a units resulting in a pK_a value of 2.7, details in Figure S2). The analysis of relevant distances shows that Asp401 interacts with its surroundings by multiple hydrogen bonds and salt bridges, which stabilize its negatively charged state. Five

https://doi.org/10.1021/acs.jctc.6c01247
J. Chem. Theory Comput. XXXX, XXX, XXX−XXX

Downloaded from pubs.acs.org/jctcce/article-pdf/doi/10.1021/acs.jctc.6c01247/6884938/acs.jctc.6c01247.pdf by UNIV OF ZURICH user on 20 October 2026

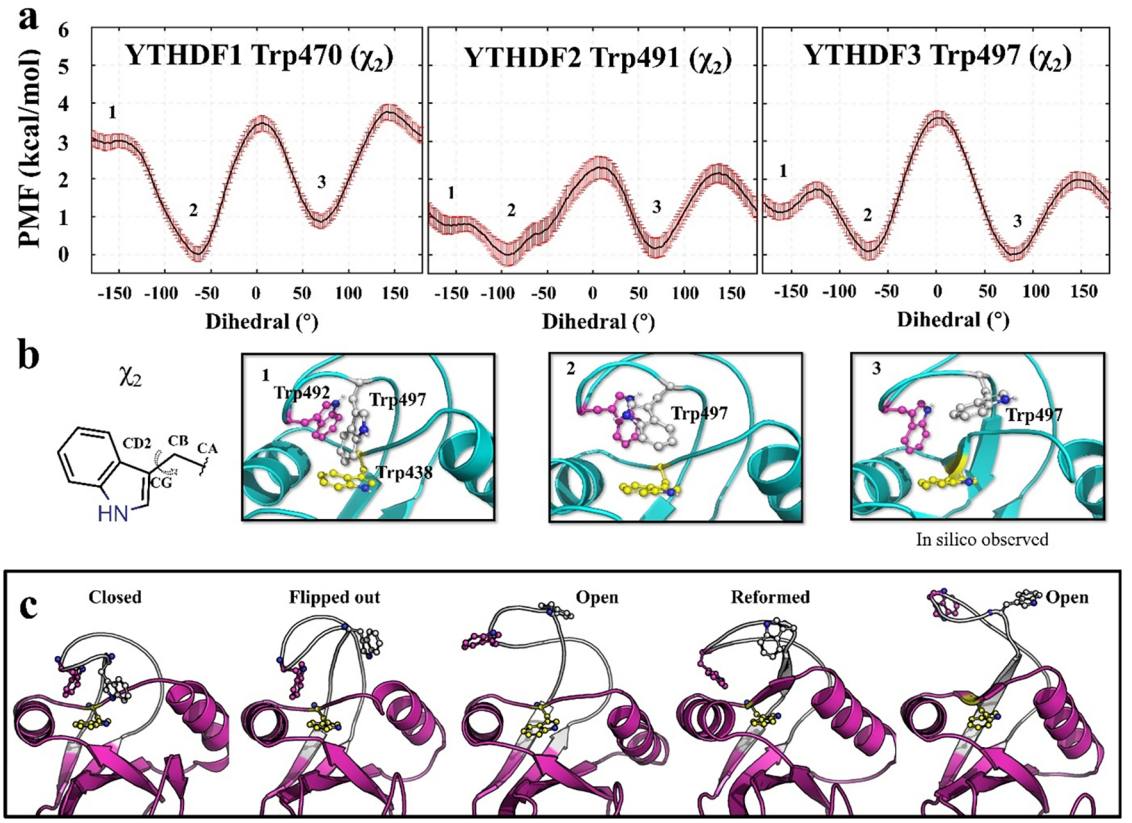


Figure 3. Local and global conformational changes of YTHDF1−3. (a) Free energy landscapes of local conformational changes for YTHDF proteins. The orientation of a tryptophan captures the conformational change during metadynamics simulations. 1: turn-off conformation; 2: turn-on conformation; 3: in silico observed conformation. (b) Three (meta-)stable conformations observed by crystal and simulation-sampled conformations. DF3 is selected as the representative to show the conformational changes, and the other two proteins have similar changes. (c) Global conformational changes of YTHDF proteins. DF3 is selected to show the large conformational changes of the Rec-loop. Two tryptophans are used to indicate the loop changes with time evolution during the simulations.

independent MD simulations of 1 μs each were then conducted on the apo system with the protonated Asp401 and the same for the deprotonated Asp401 (Figure S3). The simulations show that the protonated Asp401 has an average interaction distance with the Rec-loop 2.7 Å larger than its negatively charged counterpart. This indicates that in the apo form, Asp401 prefers the charged state and interacts with the Rec-loop in the closed conformation, ready for m^{6}A binding.

Finally, we used quantum mechanics/molecular mechanics (QM/MM) simulations[38] to determine the location of the proton. The proton shuttling was mapped onto a potential of mean force (PMF) profile (Figure 2b), showing that the proton preferentially associates with N1 of m^{6}A (−4 kcal/mol reaction free energy). Thus, the positively charged m^{6}A can form a salt bridge with the deprotonated Asp401. A 17 kcal/mol activation free energy prohibits swapping the proton from m^{6}A to Asp401. Additionally, the positively charged m^{6}A nucleobase forms cation-π interactions with three tryptophan residues of the aromatic cage. The three DF paralogs adopt highly similar overall folds in their closed conformations, with their m^{6}A-binding pockets virtually superimposable (Figure 1c). Structural alignment of the m^{6}A-RNA complexes (PDB: 4RCJ for DF1, 7Z26 for DF2, and 6ZOT for DF3) reveals an identical mode of ligand recognition. Consequently, the mechanistic principles elucidated for DF1 are expected to be valid also for DF2 and DF3.

Conformational Heterogeneity of YTHDF Proteins and Their Thermodynamic Parameters of Binding to m^{6}A-RNA

The m^{6}A-binding domain of the DF1−3 proteins has a common conformation when it binds to m^{6}A (referred to here as the closed conformation), but different conformations are observed in the apo state. In the apo state, the conformational heterogeneity of the recognition loop (Rec-loop, residues 455−472 in DF1) is consistent with the variability in four of the 18 residues of the Rec-loop (Figure S1). Our new crystal structure (PDB code 8BS4, 2.1 Å resolution) reveals that the Rec-loop of DF1 can form a two-turn α-helix in the segment Thr460-Ser466 (Figure 1c). The Rec-loop of DF3 (PDB code 8BS5, 2.49-Å resolution) can fully expose to solvent, adopting an extended open conformation, which in the crystal structure is stabilized by another monomer of the neighboring asymmetric unit (Figures 1c and S4).

We employed ITC for quantifying the thermodynamic parameters of binding of DF1−3 to the m^{6}A-RNA recognition motif, i.e., the RNA pentanucleotide GG(m^{6}A)CU. We conducted the ITC experiments at pH = 5 because m^{6}A-containing RNAs have a stronger binding affinity with DF1−3 at acidic pH values. This gave us a better chance to obtain a sigmoidal titration curve and thus enabled us to decompose the enthalpic and entropic terms accurately. Both contributions to the binding equilibrium are presented in Table 1 and Figure S5. Consistent with previous measurements by microscale thermophoresis (MST) at pH = 7.4,[14] DF1−3 display nearly

Downloaded from pubs.acs.org/jctce/article-pdf/doi/10.1021/acs.jctc.6c01247/6884938/acs.jctc.6c01247.pdf by UNIV OF ZURICH user on 20 October 2026

https://doi.org/10.1021/acs.jctc.6c01247
J. Chem. Theory Comput. XXXX, XXX, XXX−XXX

identical binding affinity to GG(m^6A)CU, with K_d values ranging from 0.6 to 0.8 μM. However, DF1 exhibits different thermodynamic parameters compared to DF2/3. DF1 has a more favorable enthalpy term (a difference of about 3 kcal/mol with respect to DF2/3), which is compensated by a higher entropic penalty. Furthermore, DF2 and DF3 share similar enthalpic and entropic contributions. These distinct thermodynamic parameters further highlight the differences among the three YTH domains. Considering the variations in sequence and structure, we assume that the differing Rec-loops of DF1−3 are primarily responsible for their different thermodynamic parameters.

We then decided to investigate the impact of the Rec-loop conformational diversity on the binding of DF1−3 to GG(m^6A)CU. To achieve this, we first introduced a disulfide bond by mutating two optimally located serines to cysteines, which was expected to lock the conformation of the proteins in their bound states. We obtained a new high-resolution crystal structure of apo disulfide-bonded DF3 (PDB code 8BS6, 1.2-Å resolution, Figure S4) which differs from the wild-type holo DF3 structure (PDB code 6ZOT)[16] by only 1.0 Å RMSD in the backbone atoms of the YTH domain (residues 405 ∼ 554). The disulfide-bonded DF1 and DF3 exhibited similar and only slightly reduced binding affinity to GG(m^6A)CU, respectively, compared to their wild-type counterparts at pH = 5 (Table 1). In contrast, the disulfide-bonded DF2 exhibited an approximately 50-fold reduction in binding affinity.

We can deduce four key points by integrating these binding data with new crystal structures. First, our strategy of introducing disulfide bonds successfully locks the closed conformation of DF1 and DF3 while minimally affecting their m^6A-binding pocket. Second, the disulfide-bond linkage may excessively rigidify the closed Rec-loop of DF2, leading to clashes with GG(m^6A)CU and impairing their binding. Third, the similar binding affinities of the disulfide-bonded DF1 and DF3 compared with their wild types suggest that the newly observed conformations (helix conformation of DF1 and open conformation of DF3) do not dominate over the closed conformation in their free forms. If they did, then the disulfide-bonded DF1 and DF3 would show a significantly different affinity because of the unfavorable conformational changes required for binding the oligoribonucleotide. Finally, the compensated binding parameters are likely influenced by subtle differences in the sequences and dynamics of their Rec-loops. In our previous study, we demonstrated that the Rec-loop of DF1 exhibits substantially greater conformational plasticity in the apo state than the corresponding loops of DF2 and DF3.[16] This enhanced flexibility is centered on the unique Gly459-Thr460-Ser461 motif in DF1, compared with Asn-Thr-Cys in DF2 and Asn-Ala-Tyr in DF3 (Figure S1), and propagates to the two tryptophan residues forming the aromatic cage. These sequence differences may therefore contribute to the exceptional conformational plasticity of the DF1 rec-loop. Consistent with this interpretation, ITC revealed a larger entropic penalty upon ligand binding for DF1 (Table 1).

Local and Global Conformational Transitions

One equivalent tryptophan, Trp470 in DF1, Trp491 in DF2, or Trp497 in DF3, plays a crucial role in determining the size of the aromatic cage (Figure 1a,b). Crystal structures of DF2 have revealed two distinct orientations of the tryptophan residue: a turn-off conformation that blocks the entrance of m^6A (PDB code 4RDO) and a turn-on conformation in the complex with m^6A (PDB code 4RDN). We performed metadynamics simulations[40] to explore the local changes of the tryptophan in the closed conformation of DF1−3 (Figure 3a,b). The free energy profiles reveal three stable conformations in all three proteins, with the turn-off conformation being less stable and facilitating the transition between the other two conformations. For example, Trp497 of DF3 adopts the turn-off conformation as an intermediate state during the transition between two equally stable orientations, bypassing a 4.5 kcal/mol free energy barrier. Interestingly, our simulations also sampled an experimentally unresolved conformation, labeled as conformation 3 in Figure 3b, which exhibits an expanded space in the m^6A binding pocket. Overall, DF1−3 displays similar local conformational changes of the tryptophan with slight differences in transition barriers (Figure 3a).

To investigate the large conformational changes of Rec-loop, we enhanced the protein dynamics of DF1−3 using Gaussian accelerated MD (GaMD) simulations,[41] starting from their closed conformations (Figure S4). We observed varying degrees of conformational changes for the Rec-loop through 1-μs simulations with five replicas for each protein. The Rec-loop dynamics was significantly amplified compared to classical MD (cMD) simulations (Figure S6). Multiple trajectories exhibited a trend of Rec-loop opening. Further extended simulations were performed on those opening-oriented trajectories, confirming that DF1−3 undergo similar local conformational changes in the aromatic cage before the Rec-loop opening. Taking DF2 as an example (Figure 3c), Trp491 undergoes significant conformational changes by flipping its side chain out of the aromatic cage, causing partial deformation of the m^6A binding site. This triggers a large conformational change of Rec-loop, with Trp486 detaching from the base of the binding pocket (around Trp432). Once the Rec-loop completely opens, it becomes highly flexible.

To validate the proposed opening mechanism of the YTHDF proteins, we simulated the reverse process, i.e., the closing of the Rec-loop. The extended conformation of DF3 is 3.6 Å RMSD away from its closed conformation (Figure S7). Using the open structure as a template, we modeled the same conformation for DF1 and DF2 and performed the MD simulations for five microseconds on all three systems to explore the Rec-loop dynamics. DF2 and DF3 exhibited quick closure of the Rec-loop (Figure S7). The rapid closure of their Rec-loops means their open conformations are merely transient. In the MD simulations, we did not observe the complete formation of the aromatic cage. Across all five independent MD simulations, Trp486 in DF2 and Trp492 in DF3 assumed first the correct orientation as in the aromatic cage. In contrast, Trp491 in DF2 and Trp497 in DF3 did not reach the orientation (Figures S8 and S9). The (partial) sequence of the event is the reverse process of the one observed in the MD runs started from the closed conformation, thus confirming the opening transition observed in the GaMD simulations (Figure S6). In contrast, DF1 did not undergo closure of the Rec-loop and instead remained flexible during the simulations started from the open conformation. These simulation results provide further evidence that DF1 has a more dynamic Rec-loop than DF2 and DF3.

Downloaded from pubs.acs.org/jctce/article-pdf/doi/10.1021/acs.jctc.6c01247/6884938/acs.jctc.6c01247.pdf by UNIV OF ZURICH user on 20 October 2026

https://doi.org/10.1021/acs.jctc.6c01247
J. Chem. Theory Comput. XXXX, XXX, XXX−XXX

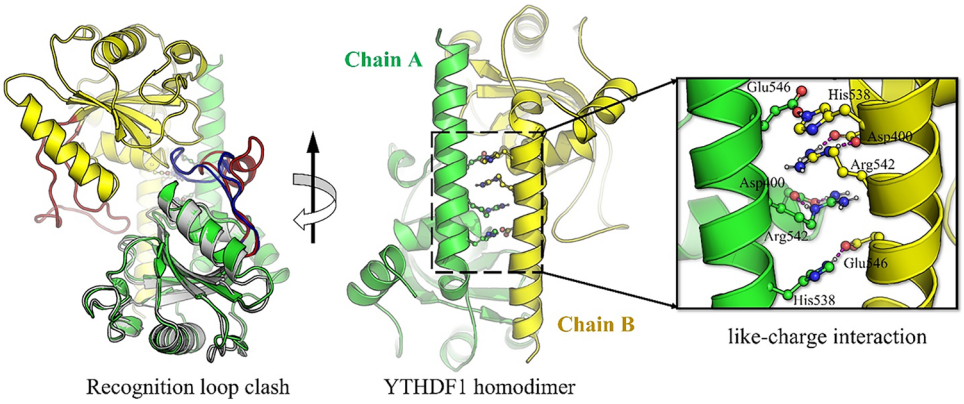


Figure 4. Structural details of the DF1 homodimer structure. (Left) Structure of DF1 (gray) with the Rec-loop (blue) in closed conformation (PDB code 4RCJ) is superposed onto chain A of the dimer structure (PDB code 8BS4, green and yellow) with the Rec-loop in open conformation (red). The Rec-loop adopts a short two-turn helical structure in chain A, and it appears disordered in chain B. (Middle and right) Details of the interactions at the dimeric interface.

Dimerization of YTHDF1 In Vitro

The crystal structures of DF1−3 reveal the presence of multiple contacting monomers in their central asymmetric units, suggesting potential models for their functional oligomerization. For instance, in one asymmetric unit, two DF1 monomers (PDB ID: 8BS4, Figure 4) interact primarily through their C-terminal α-helices in an antiparallel orientation. To investigate the possibility of dimerization in vitro, we performed gel filtration chromatography at pH = 7.4. Interestingly, only DF1 exhibits a peak in the dimerization range (46 kDa, 55 mL in Figure S10), and the same peak does not appear for DF2 and DF3. Notably, the homodimer of DF1 dissociates at pH = 5.0. To quantify the strength of DF1 dimerization, we performed dilution ITC experiments, which yielded a K_d of 37 μM (Figure S10), consistent with transient homodimerization in vitro. Notably, the local concentrations of YTHDF proteins within liquid−liquid phase-separated condensates may reach the high-micromolar to millimolar range.[42] Such elevated local concentrations could shift the equilibrium toward the dimeric state, potentially favoring DF1 homodimerization within condensates.

To validate the DF1 dimer model suggested by the crystal structure of the wild type (PDB code 8BS4), we focused on Arg542 and His538, which seemingly stabilize the dimerization interface. These residues engage in "like-charge" pairing interactions,[43] with the guanidinium side chains of two Arg542 residues from different monomers stacking together, while the neighboring His538 contributes to charge-repulsive stacking. To assess the structural stability of these interactions, we performed comparative MD simulations on two systems: one with neutral His538 and the other with positively charged His538 mimicking neutral and low pH conditions, respectively (Table S2). The simulations revealed that the system with neutral His538 exhibited a stable dimer interface, whereas the two dimer helices tended to separate under the low pH condition (protonated His538) (Figure S11). To further investigate the protonation behavior of His538 at the dimer interface, we performed constant pH molecular dynamics (cpHMD) simulations to estimate its pK_a values (see the Methods section). The calculated pK_a values were 6.5 for His538 on chain A and 5.6 on chain B (Figure S12). These results suggest that at pH 5, both histidine residues are predominantly protonated, which disfavors dimerization due to electrostatic repulsion. In contrast, at pH 7, deprotonation of the histidine side chains reduces this repulsion, thereby favoring dimer formation. Encouraged by these simulation results, we introduced alanine mutations separately to Arg542 and His538 and measured the dimerization tendency of the mutants. As expected, neither mutant could form a homodimer according to gel filtration and dilution ITC measurements at pH = 7.4 (Figure S10). Together, the simulation results and mutagenesis experiments provide additional support for the validity of the dimeric model represented by the crystal structure 8BS4. Moreover, they highlight the critical role of the C-terminal α-helix in stabilizing the dimer interface and facilitating dimer formation.

We next tried to answer the question of why only DF1 can form a homodimer despite the highly homologous YTH domains shared by all three paralogs. In the dimeric structure of DF1 (PDB code 8BS4), the Rec-loop adopts a short (two-turn) helical structure in chain A (Figure 4), while it appears disordered in chain B. Upon analyzing the different conformations, we observed that when the Rec-loop assumes the closed conformation, it pushes away the other monomer, thereby preventing dimer formation (Figure 4). This led us to hypothesize that the helical Rec-loop may be essential in facilitating dimerization. To test this hypothesis, we first purified the disulfide-bonded DF1 variant that forced the Rec-loop to close. As expected, unlike the wild-type construct, we did not obtain a dimerization peak in the gel filtration (Figure S10). This result indicates that the closed conformation prohibits dimerization.

Interestingly, the helical Rec-loop was observed only in the DF1 crystal structure, but not in those of DF2 or DF3. To investigate whether DF2 and DF3 can adopt the helical Rec-loop, we generated homologous models using the monomer of DF1 (chain A of 8BS4, Figure 1c) as a template. Subsequently, we performed five independent 1-μs MD runs on DF1−3 starting from the presence of the helical structure. The Rec-loop deviated by only 1.4 Å from the crystal structure in DF1. For DF2 and DF3, the originally helical loop deviated by 2.5 Å and 2.4 Å, respectively (Figure S13). Moreover, the average structure of DF1 exhibited a higher helical content in its Rec-loop than those of DF2 and DF3. These findings suggest that the helical loop is more stable in DF1 than in DF2 and DF3, thereby supporting the notion that the stable helical structure

Downloaded from pubs.acs.org/jctce/article-pdf/doi/10.1021/acs.jctc.6c01247/6884938/acs.jctc.6c01247.pdf by UNIV OF ZURICH user on 20 October 2026

https://doi.org/10.1021/acs.jctc.6c01247
J. Chem. Theory Comput. XXXX, XXX, XXX−XXX

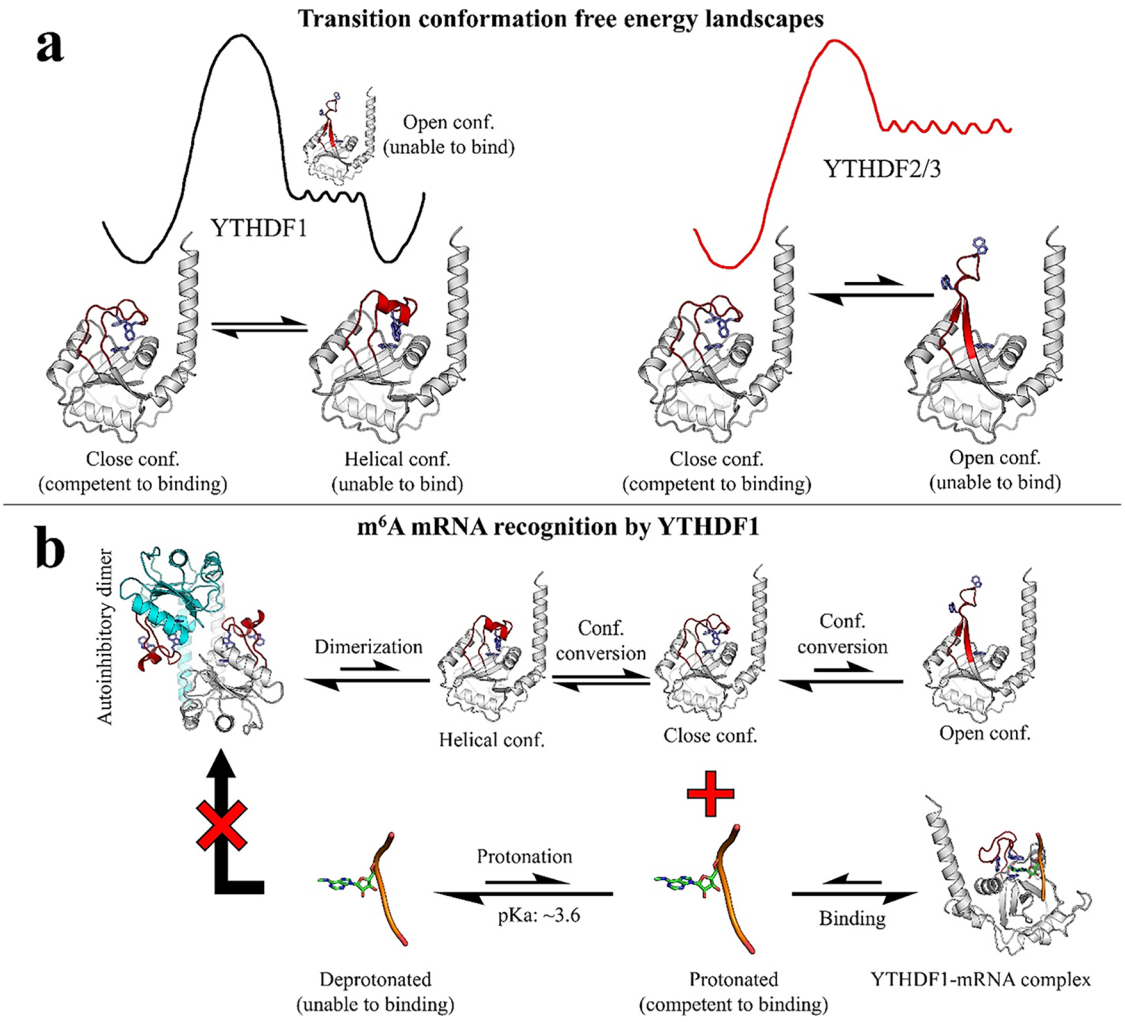


Figure 5. Schematic models of the (a) free energy landscape of Rec-loop conformational changes in DF1 (left) and DF2/3 (right) and (b) the mechanism of DF1 autoinhibition by dimerization. The dimerization equilibrium in (b) is concentration-dependent.

of Rec-loop facilitates the homodimerization of DF1, but this mechanism does not apply to DF2 and DF3.

Next, we aimed to explore whether slight sequence differences in the C-terminal long helices affect the dimerization of YTHDF proteins. We constructed homologous dimer models for DF2 and DF3 using the dimer structure of DF1 as a template. We performed five independent 200 ns MD runs on the three dimer systems, revealing that DF1 exhibits a more pronounced interacting area between the two monomers than DF2 and DF3 (Figure S11). The area of the interacting surface is 604 Å^2, 502 Å^2, and 491 Å^2 on average for DF1, DF2, and DF3, respectively. Furthermore, the analysis of MD trajectories confirmed that DF1 displayed more stable dimer C-terminal helix−helix interactions than DF2 and DF3.

In short, the homodimer structure of DF1 suggests an autoinhibitory model in which the accessibility of m^{6}A-RNAs to the aromatic cage is blocked (Figure 4). We compared the binding affinities of wild-type and dimerization-disabled R542A to GG(m^{6}A)CU at pH = 7.4 and found that the wild type cannot bind to the oligonucleotide, while the point mutant R542A (dimer-destabilizing mutant) shows a K_d of 108 μM (Table S1). This comparison supports the proposed autoinhibitory model.

DISCUSSION

Recognition Loop Dynamics Distinguishes the m^{6}A-RNA Reader Domains of the YTHDFs

The 18-residue Rec-loops of DF1−3 differ in only four residues (Figure S1). Although the subtle sequence difference does not confer the three paralogs with differential affinity for m^{6}A, they do redistribute the binding enthalpy and entropy (Table 1). Notably, DF1 achieves the most favorable binding enthalpy (−16.4 kcal/mol) among the three paralogs when binding to GG(m^{6}A)CU. One possible explanation is that the presence of a glycine and serine in the variable 3-residue segment of DF1 (Gly459-Thr460-Ser461) allows for a more flexible adaptation to the m^{6}A-RNA binding than the corresponding three-residue segments in DF2 (Asn-Thr-Cys) and DF3 (Asn-Ala-Tyr). This argument is supported by comparing Rec-loops in the closed conformational states of DF1−3. DF1 shows the most pronounced local dynamics on its Rec-loop.[16]

Our crystal structures provide evidence that the Rec-loop of DF1 can adopt a stable two-turn helical structure, whereas DF2 and DF3 cannot (Figures 1 and S13). In this conformation, the m^{6}A binding pocket is fully exposed to the solvent, resulting in a distinct protein fold compared to its closed conformation. Figure 5a illustrates alternative stable conformational states of

https://doi.org/10.1021/acs.jctc.6c01247
J. Chem. Theory Comput. XXXX, XXX, XXX−XXX

Downloaded from pubs.acs.org/jctcce/article-pdf/doi/10.1021/acs.jctc.6c01247/6884938/acs.jctc.6c01247.pdf by UNIV OF ZURICH user on 20 October 2026

DF1 (helical Rec-loop), separated by a free energy barrier within a dynamic free energy landscape following the opening of its Rec-loop. In contrast, DF2 and DF3 predominantly adopt a single stable closed conformation, and their Rec-loops exhibit a relatively rigid conformation. Even though it transiently opens, it rapidly returns to the closed form (Figures S7 and S8).

Atomistic-Level Mechanisms of YTHDF Proteins Recognizing m^{6}A-RNA

Crystal structures have revealed similarities in how DF proteins recognize GG(m^{6}A)CU. For example, a hydrogen-bond distance was observed between the side chain of Asp401 in DF1 (Asp422 and Asp428 for DF2 and DF3, respectively) and the N1 nitrogen of m^{6}A. Our FEP and QM/MM calculations uncover that the aspartic acid is negatively charged while N1 of m^{6}A is protonated, resulting in a favorable polar interaction (Figure 2). Additionally, the positively charged m^{6}A forms π-π and cation-π interactions with the three tryptophane side chains in the aromatic cage. These interactions partially compensate for the unfavorable protonation state of m^{6}A. Nonetheless, the binding enabled by these interactions is approximately 14-fold weaker than that of the Asp401Asn mutant of DF1 at pH 7.4.[17] This asparagine residue is also present in YTHDC1 and forms a typical hydrogen bond with m^{6}A (Figure 1a). The asparagine side chain introduced in the Asp401Asn mutant forms a conventional hydrogen bond with the neutral m^{6}A base (Figure 1a). In contrast, the corresponding aspartic acid in DF1−3 weakens m^{6}A binding at physiological pH due to its low degree of protonation, which limits its ability to engage in strong hydrogen bonding. These distinct hydrogen-bonding modes underlie the intrinsic difference in m^{6}A-RNA recognition between DF1−3 and YTHDC1. Importantly, we observed that lowering pH significantly enhances the binding affinity of DF1−3 for m^{6}A-modified RNAs (Table 1). For example, DF1 exhibits an approximately 20-fold increase in affinity when the pH is reduced from 7.4 to 5.0. This enhancement is likely due to increased protonation of either the aspartic acid residue or the m^{6}A base under acidic conditions. cpHMD simulations could provide deeper insight into the dynamic coupling between Asp401 of DF1 and the m^{6}A moiety during proton transfer.[44−48] However, their application is currently limited by the lack of validated parameters for the protonated m^{6}A. Developing these parameters and incorporating protonated m^{6}A into future simulations will therefore be an important next step.

The aromatic cage regulates the access of m^{6}A through a local conformational change of a tryptophan residue in the binding pocket, specifically Trp470, Trp491, and Trp497 in DF1, DF2, and DF3, respectively. Our metadynamics simulations deny an "on−off" switch for the entry of m^{6}A to the aromatic cage (Figure 3a). This observation is consistent with our soaking experiments on DF2,[15] where the "turn-off" conformation of Trp491 can transform into the "turn-on" conformation upon ligand binding. These results suggest that this tryptophan residue stabilizes the aromatic cage by switching between multiple (meta)stable conformations rather than an "on−off" switch. Furthermore, the newly discovered conformation, i.e., conformation 3 in Figure 3b, enlarges the m^{6}A binding pocket and thereby provides opportunities for exploring new chemical types as potential binders. For the global conformational changes, the model shown in Figure 5a nicely illustrates the similarity and difference in the free energy surface of DF1 with respect to DF2/3. Importantly, the differential dynamics of Rec-loops provide an opportunity to design selective inhibitors, as demonstrated in a case about selective inhibitors for FGFR2 over its highly homologous members.[49] In fact, our recent studies have shown that small-molecule binders can achieve more than 10-fold selectivity between DF1−3.[50]

DF1 exhibits a unique inhibitory homodimerization in vitro. Two structural factors distinguish the dimerization capacity of DF1−3: the long α-helix at the C-terminus and the Rec-loop. First, the two monomers of DF1 align their C-terminal α-helices in an antiparallel manner, forming the dimerization interface. The interface is finely tuned by a charge-like arginine-arginine stacking, and the interaction is further stabilized by the surrounding residues. This like-charge interaction appears to be conserved in DF1−3, with minor variations in other regions of the long helix (Figure S1). Nonetheless, these subtle sequence alterations could perturb the DF2/3 dimer interface (Figure S11). Our in vitro experiments, together with structural modeling, demonstrate that dimer formation is favored under neutral pH conditions and disfavored in an acidic environment. His538 functions as a pH-sensitive regulatory residue, modulating dimerization in response to changes in protonation state. Second, the two-turn helical structure in the Rec-loop of DF1 facilitates its dimer formation by avoiding clashes between the two monomers (Figure 4). The alternative conformation of Rec-loop is only stable in DF1 (Figure S13). By contrast, DF2/3 quickly revert their open Rec-loop back to the closed form, thereby preventing dimer formation (Figure S7).

Building on insights from this and previous studies, we propose an integrated model for the recognition of m^{6}A-modified RNA by YTHDF proteins (Figure 5b). DF1−3 dynamically alternate between open and closed conformations, with distinct conformational dynamics observed in their Rec-loops. In the closed conformation, the Rec-loop adopts a configuration that enables high-affinity binding to m^{6}A-modified RNAs. For a functional RNA, the presence of the m^{6}A modification promotes a solvent-exposed orientation of the modified adenosine, enhancing accessibility for recognition.[34] Occasional protonation at the N1 position of m^{6}A can generate a positively charged species, which is specifically recognized by a conserved aspartic acid residue in the m^{6}A binding pocket. This interaction is further stabilized through a network of favorable contacts, including salt bridges, hydrogen bonds, and cation−π interactions. Transition of the Rec-loop into the open conformation disrupts this recognition, facilitating the dissociation of the m^{6}A-RNA complex. Notably, DF1, unlike DF2 or DF3, adopts an alternative open conformation in which the Rec-loop forms a short α-helical segment. This unique structural feature promotes homodimerization of DF1, which sterically occludes the m^{6}A binding site and thereby inhibits RNA binding.

Implications for Biological Functions and Carcinogenesis

Our findings highlight the crucial role of acidity in the binding of m^{6}A-RNAs to DF1−3 in vitro. Lower pH values enhance their binding affinity by facilitating the protonation of m^{6}A or disrupting the dimerization interface. These in vitro experiments indicate that the local intracellular pH could influence cellular functions mediated by cytoplasmic DF1−3. Although the average cytosolic pH is buffered and maintained at 7.1−

Downloaded from pubs.acs.org/jctce/article-pdf/doi/10.1021/acs.jctc.6c01247/6884938/acs.jctc.6c01247.pdf by UNIV OF ZURICH user on 20 October 2026

https://doi.org/10.1021/acs.jctc.6c01247
J. Chem. Theory Comput. XXXX, XXX, XXX−XXX

7.2, pH values can vary significantly in different organelles.[51] Moreover, the intracellular pH gradient is altered in cancer cells, leading to metabolic changes and tumorigenesis.[52] Since DF proteins function as regulators of translation or degradation for various m^{6}A-RNAs, their binding status likely plays a critical role in these cellular processes. Investigating the effects of acidity on cell functions, similar to other factors such as oxidative stress,[53] could be a future research direction. In such studies, new spatiotemporally resolved pH imaging techniques[54] would be required.

In vitro studies have demonstrated that DF1 can transiently form homodimers via their YTH domains. Colocalization can increase local protein concentration from the μM to mM range.[42] DF proteins can undergo low-complexity domain-driven liquid−liquid phase separation (LLPS) at the μM level,[20] leading to a more condensed environment. The condensation of DF paralogs is facilitated by nonspecific contacts mediated by low-complexity segments,[20] and the presence of multiple m^{6}A-modified RNAs further promotes this process by specific protein tethering.[21] Within this context, the proposed inhibitory dimerization of DF1 may provide an additional regulatory mechanism that modulates m^{6}A-RNA recognition among the three YTHDF paralogs. Several clinical mutants located near the dimerization helix, such as Arg542, His538, and Glu546, have been reported in various cancers, as documented by ICGC, TCGA, and COSMIC databases.

Importantly, our dimer structure shows a ligandable pocket with a volume of 662 Å^3, as measured by fpocket,[55] offering a platform for exploring novel types of binders (Figure S14). According to this model, potential binders could act as stabilizers of the dimerization (general molecular glue), converting the transient dimer into a more permanent one. Such stabilizers could exhibit selectivity among DF paralogs and thus contribute to understanding their specific biological functions and potentially serve as therapeutic agents for treating cancers. Recently identified covalent inhibitors, binding to the same dimerization interface, further validate our proposal.[56]

Finally, our engineered disulfide-linked DF1/3 mutants successfully stabilized the proteins in a closed conformation competent for m^{6}A-RNA binding. These conformationally constrained mutants provide a useful tool for investigating cellular functions associated with m^{6}A-RNA recognition while minimizing potential contributions from alternative conformational states of YTHDF proteins. Collectively, the mechanistic insights, molecular models, and biochemical tools developed in this study provide a foundation for further investigating the functional roles of DF1−3 in living cells.[11,57]

Conciliating the Redundancy-Specificity Debate

The unified model proposes that DF1−3 bind largely overlapping populations of m^{6}A-modified mRNAs rather than distinct transcript subsets and that their predominant shared function is to promote mRNA degradation rather than translation.[14] This view is based primarily on transcriptome-wide reanalysis showing extensive overlap in YTHDF target binding and on the conclusion that all m^{6}A sites can be engaged by all three paralogues with similar binding ability.

Our results are broadly consistent with this framework at the level of bound-state recognition. DF1−3 form nearly identical complexes with m^{6}A-containing RNA[15−17] and display similar overall binding affinity, indicating that the three paralogs converge on a common m^{6}A-bound structural end point. However, our data also show that the strongest version of the unified model is overreductive. In its strictest form, this model implies that DF1−3 bind m^{6}A equivalently and therefore function as mechanistically interchangeable readers. Our observations do not support such a fully redundant view. Instead, the distinct thermodynamic signatures, apo state conformations, and oligomerization properties of the three paralogs demonstrate that despite adopting a similar RNA-bound structure, they are not physically identical molecular machines. Thus, redundancy appears to apply primarily to the final bound-state recognition, whereas paralog-specific behavior may also be encoded in the conformational and self-assembly landscapes.

Conversely, the original specificity model,[9,11,13] which implied that each paralog recognizes distinct m^{6}A-RNA cohorts and recruits specific machineries for those biological functions, is difficult to reconcile with the substantial overlap in m^{6}A-site binding reported by the unified-model studies and subsequent work.[14,58,59] Recent studies have already tamped this strict specificity view by showing that structural differences in low-complexity regions (LCRs) and disorder-related properties can give rise to distinct cellular functions. Our data add several new layers to the framework. Even within the highly conserved and structurally ordered YTH domain, DF1−3 can still be distinguished by their different binding mechanisms toward the same m^{6}A-containing RNAs, their distinct responses to pH, and their different assembly properties. These findings suggest that functional divergence among YTHDF paralogs may arise not only from their highly variable LCRs but also from subtle differences within their otherwise highly conserved YTH domains.

Taken together, our results support a hybrid model in which the three YTHDF paralogs are redundant in terms of the bound-state m^{6}A recognition yet nonredundant in the conformational and assembly landscapes. This framework provides a molecular rationale for why YTHDF proteins can appear to be interchangeable in some settings while exhibiting distinct biological behaviors in others.

Future Directions

Our thermodynamic data show that DF1−3 bind the same m^{6}A-containing RNA with similar overall affinity but distinct enthalpic and entropic contributions, indicating that the three paralogs reach a common bound-state through different energetic pathways. Given the conformational plasticity of YTH domains and the dynamic differences, their association and dissociation kinetics are also likely to be different. Quantitative kinetic measurements, such as biolayer interferometry (BLI) or surface plasmon resonance (SPR), should therefore be performed to determine k_{on} and k_{off} and to test whether these thermodynamic differences translate into distinct binding kinetics, despite a shared RNA-bound structure. In future kinetic studies, longer RNA substrates, both with and without m^{6}A modification, should be examined to better recapitulate molecular recognition under physiologically relevant conditions.

A second priority is to define the conformational dynamics underlying the energetic differences. High-resolution solution NMR should be particularly informative for comparing the apo and RNA-bound states of the three paralogs and for mapping local flexibility, especially within the Rec-loop. Because our data suggest that the major divergence among YTHDF proteins lies in the free-state conformational landscape rather

Downloaded from pubs.acs.org/jctce/article-pdf/doi/10.1021/acs.jctc.6c01247/6884938/acs.jctc.6c01247.pdf by UNIV OF ZURICH user on 20 October 2026

https://doi.org/10.1021/acs.jctc.6c01247
J. Chem. Theory Comput. XXXX, XXX, XXX−XXX

than in the final bound complex, such measurements will be essential for clarifying how each paralog accesses the m^{6}A-bound state. The engineered disulfide-linked YTHDF proteins developed here should provide useful reference states for these analyses.

We also identified DF1 homodimerization. This assembly should next be validated in cells using orthogonal approaches, such as bimolecular fluorescence complementation (BiFC), fluorescence resonance energy transfer (FRET), or proximity labeling. Its functional significance is of particular interest because YTHDF proteins undergo phase separation in vitro and in cells, and multivalent m^{6}A-modified RNAs enhance this behavior by bringing their LCRs into proximity. It will therefore be important to determine whether DF1 dimerization affects the condensation or client protein recruitment and whether this property distinguishes DF1 from DF2 and DF3 in cellular functions. Because we identified a cavity at the core of the DF1 dimer interface, the structure-guided development of a small-molecule dimer stabilizer could also provide a useful chemical tool for probing the cellular consequences of DF1 self-association.

Finally, both m^{6}A-RNA binding and DF1 dimerization were highly sensitive to the pH in our in vitro assays. These findings suggest that protonation may regulate the prebinding ensemble and higher-order assembly of DF proteins under biologically relevant conditions. Future studies should therefore test whether local or transient pH changes in cells influence DF-RNA binding, oligomerization, or condensation behavior. Such experiments will be essential to determine whether the pH dependence observed in vitro is recapitulated in cellular and physiological settings and, more broadly, to define how environmental cues shape the balance between redundancy and specificity within the YTHDF family.

CONCLUSIONS

We have carried out a combined experimental and simulation study of the m^{6}A-RNA reader domains of DF1−3, focusing on their structures, binding thermodynamics, and Rec-loop dynamics. We found that DF1−3 exhibit similarities when they assume conformations with closed Rec-loops. They interact with m^{6}A via the same electrostatic interaction between a negatively charged Asp side chain and the N^1-protonated, i.e., positively charged m^{6}A in the aromatic cage. In addition, DF1−3 have in common the cation-π interactions with the three tryptophane side chains of the cage. Also, DF1−3 show similar dynamics in the closed Rec-loop state and a common opening mechanism of the Rec-loop. These similarities explain why they have similar affinity to m^{6}A-RNA and perform certain redundant cell functions. However, notable differences emerge when their Rec-loops are open. Unlike DF2/3, DF1 can adopt an alternative stable conformation with a two-turn helix in the Rec-loop that does not hinder homodimerization. The opening of the Rec-loop in DF1 also displays more pronounced flexibility, while the Rec-loop of DF2/3 rapidly reverts to the closed conformation, which prevents homodimerization. Furthermore, to further investigate the thermodynamic parameters of binding of individual DF paralogs, we have employed point mutagenesis of two spatially adjacent Ser side chains, which were mutated to Cys to lock the closed state of the cage by a disulfide bond. The informations on the new conformations, dimer model of DF1, engineered proteins, and Rec-loop dynamics present opportunities to develop selective binders, which can be used as chemical probes for exploring cellular functions and related diseases.

MATERIALS AND METHODS

Cloning, Protein Expression, and Purification

The human YTHDF1 YTH domain (amino acids 361−559), the YTHDF2 YTH domain (amino acids 383−579), and the YTHDF3 YTH domain (amino acids 387−585 and amino acids 387−567) were subcloned into a pET-based vector harboring N-terminal hexa-histidine tag and a TEV cleavage site. All recombinant proteins were overexpressed at 24 °C in *E. coli* BL21 (DE3) and purified by HiTrap nickel column. The His tag was cleaved by the addition of TEV protease (1:100) to the purified recombinant protein, followed by dialysis to remove imidazole at 4 °C overnight. The samples were then passed through a nickel column and further purified by size exclusion chromatography. The final gel filtration buffer was 20 mM Tris pH 7.4 and 150 mM NaCl for neutral pH experiments and 20 mM sodium acetate pH 5 and 150 mM NaCl for acidic pH experiments.

The following primers were used to generate the mutants.

DF1 S398C For: ATCAAGAGCTACTGTGAGGACGACATCCACCGC

DF1 S398C Rev: GATGTCGTCCTCACAGTAGCTCTTGATGATGAAC

DF1 S466C For: GCCGGGGTCTGGTGTCAGGACAAGTGGAAG

DF1 S466C Rev: CCACTTGTCCTGACACCAGACCCCGGCACTG

DF2 S419C For: ATTAAGAGCTACTGTGAGGACGATATTCACCGTTC

DF2 S419C Rev: AATATCGTCCTCACAGTAGCTCTTAATGATGAAAAC

DF2 S487C For: GCAGGTGTGTGGTGCCAGGACAAATGGAAGGGTC

DF2 S487C Rev: CCATTTGTCCTGGCACCACACACCTGCACATGTG

DF3 S425C For: GCTACTGTGAGGATGACATACATCGTTCC

DF3 S425C Rev: CCTGCACACAAATATTAATTTTCGATGACACTC

DF3 S493C For: GTCTGGTGTCAGGATAAGTGGAAGGG

DF3 S493C Rev: GCATACGACCACAGACCACAGTCC

DF1 H538A For: CTTTGCTGCCTACGAGAAGCGCCAGGAGGAGGAGGAGG

DF1 H538A Rev: CTCGTAGGCAGCAAAGTCGTCGAAGATGGAGGTTGTGTG

DF1 R542A For: AAGGCCCAGGAGGAGGAGGAGGTGGTGCGCAAG

DF1 R542A Rev: CTCCTGGGCCTTCTCGTAGTGAGCAAAGTCGTCGAAGATGGAGG

Crystallography

All crystals were obtained using hanging drop vapor diffusion at 22 °C with a protein concentration of 10 mg/mL. 8BS4 (DF1_Dimer, amino acids 361−559) was crystallized in 2 M ammonium citrate. 8BS5 (DF3 open, amino acids 387−567) was crystallized in 0.2 M potassium sodium tartrate and 20% PEG 3350. 8BS6 (dsDF3, amino acids 387−585) was crystallized in 2.1 M sodium malonate. The crystals were harvested and frozen in liquid nitrogen with an additional 20% glycerol as cryoprotectant.

Downloaded from pubs.acs.org/jctcce/article-pdf/doi/10.1021/acs.jctc.6c01247/6884938/acs.jctc.6c01247.pdf by UNIV OF ZURICH user on 20 October 2026

https://doi.org/10.1021/acs.jctc.6c01247
J. Chem. Theory Comput. XXXX, XXX, XXX−XXX

The refinement procedure basically followed one of our previous publications.[33] Diffraction data were collected at the Swiss Light Source (Villigen, Switzerland) using beamline X06DA (PXIII) and processed using XDS. The structures were solved by molecular replacement using the Phaser program from the Phenix package. Apo DF1 (PDB ID: 4RCI) was used as a search model. The model building and refinement were performed using COOT and Phenix.refine. Data collection and refinement statistics are summarized in Table S3.

Coordinates

The atomic coordinates and structure factors for the three crystal structures have been deposited in the Protein Data Bank (PDB) with the accession codes 8BS4 (dimer DF1 structure), 8BS5 (DF3 with an open Rec-loop), and 8BS6 (disulfide-bond DF3).

Binding Assay

Isothermal titration calorimetry (ITC) experiments were carried out at 25 ^{0}C using MicroCal ITC200 (GE Healthcare). All ITC experiments were performed in gel filtration buffer (20 mM Tris-HCl at pH 7.4 and 150 mM NaCl or 20 mM sodium acetate at pH 5 and 150 mM NaCl). GG(m^{6}A)CU was dissolved at 500 μM in the buffer and titrated into the sample cell containing the protein at 50 μM. After an initial injection of 0.4 μL, 19 injections of 2.0 μL each were performed. For dilution ITC experiments, 500 μM protein samples in pH 7.4 buffer were loaded into a syringe and then injected into the same buffer. The raw data were integrated and analyzed using the MicroCal Origin software package.

Model Building

A total of 17 molecular systems were constructed based on previously published and newly released structures. These systems include 14 apo systems, one holo system, and two unphysical hybrid systems. Their detailed information is summarized in Table S2.

We take the apo structure YTHDF3 with the open Rec-loop as an example to describe our general model-building procedure. The original coordinates, including protein and crystal water molecules, were extracted from the structure 8BS5. The hydrogen atoms were added by the CHARMM program (version 42b2),[60] and the protonation states were determined at neutral pH conditions. Further details about protonation states are listed in Table S2. The complex system was solvated in a rhombic dodecahedron (RHDO) TIP3P[61] water box with a lattice length of 75 Å to ensure a 12 Å buffer space between the protein atoms and the boundary of the water box. To neutralize the system and mimic the physiological conditions, we added Na+ and Cl- ions at a 0.15 M concentration to the bulk water of the solvated system. Other apo, holo, and dimer systems were trimmed similarly to the YTHDF3 system with varied numbers of water molecules and salt atoms.

The conformation with the Rec-loop opened was generated by homology modeling for YTHDF1 and YTHDF2. We used the crystal structure 8BS5 of YTHDF3 as the template to capture the open conformation of the Rec-loop. SWISS-MODEL[62] was used for model building via its default homology modeling method provided on the website (https://swissmodel.expasy.org). Similarly, another two homology models for YTHDF2−3 with helix Rec-loops were constructed by taking the crystal structure 8BS4 of YTHDF1 as the template.

Two dimer models for YTHDF2−3 were modeled by using the dimer structure 8BS4 of YTHDF1 as the template. We employed MODELER 10.2[63] to build the homology model and thereby consider interactions between the two monomers. The "AutoModel" procedure was used for the modeling, and the default setting was implemented. Missing coordinates, especially for the Rec-loop of chain B in structure 8BS4, were built and refined by MODELER 10.2. The final model was selected according to the best DOPE score.

Conventional (Unbiased) Molecular Dynamics Simulations

Each simulation system was initially minimized for 10,000 steps under a series of restraints and constraints on the protein atoms to release its poor contacts and geometry presented in the original crystal structure. The minimized structure was heated to 300 K and equilibrated in an NVT condition (constant volume and temperature) and was further equilibrated by switching to an NPT condition (constant pressure and temperature). All the equilibration phases lasted for one nanosecond (ns) using the CHARMM program (version 42b2).[60] A further continued 10 ns equilibration and 1000 ns production runs were carried out in NPT conditions using the NAMD program (version 2.14).[64] The pressure was controlled by the Nosé-Hoover Langevin piston method with a 200 ps (ps) piston period and a 100 ps piston decay time.[64−66] The temperature was maintained at 300 K using the Langevin thermostat with a 5 ps friction coefficient. The integration time step was set to 2 fs by constraining all the bonds involving hydrogen atoms by the SHAKE algorithm. van der Waals interaction energies were calculated using a switching function with a switching distance from 10 to 12 Å,[67] and electrostatic interactions were evaluated using the particle mesh Ewald summation (PME) method.[68] Lennard-Jones long-range correction was enabled.[69]

The CHARMM36 force field[70] was used to describe the protein. Five independent runs (1000 ns for each) with random initial velocities were carried out for each system, resulting in 5 μs (μs) sampling time. MD snapshots were saved every 20 ps along the trajectories for further analysis. Geometric measurements, for example, dihedral angles, distances, and root-mean-square deviation (RMSD), were performed with CHARMM routines. All statistical analyses were done in MATLAB (Version 2021b);[71] structural figures were generated with the PyMOL graphic software (Version 2.5.2),[72] intra/interaction analyses and residue mutations were performed via Maestro (Version 11.5).[73]

pK_a Calculations by Alchemical Simulations

We used the alchemical free energy simulation method to determine the pK_a shift of Asp401 from water to YTHDF1. A thermodynamic cycle was designed to reduce the computational expense (Figure 2a). Instead of physically simulating folding and unfolding events (vertical arms in Figure 2a), an unphysical pathway (horizontal arms in Figure 2a) was conducted. Because the natural unfolding to the folding process of YTHDF1, i.e., exposing Asp401 to bulk water or its inverse event, is not the focus, such alchemical simulations enable us to enhance sampling dynamics of the systems, therefore producing accurate thermodynamic quantities, namely the free energy difference caused by the deprotonation/protonation ($\Delta\Delta G$). The pK_a shift of Asp401 and its pK_a value in YTHDF1 were then calculated.

A hybrid residue presenting deprotonated and protonated Asp401 (pAsp401) simultaneously was constructed, and two

Downloaded from pubs.acs.org/jctce/article-pdf/doi/10.1021/acs.jctc.6c01247/6884938/acs.jctc.6c01247.pdf by UNIV OF ZURICH user on 20 October 2026

https://doi.org/10.1021/acs.jctc.6c01247
J. Chem. Theory Comput. XXXX, XXX, XXX−XXX

side chains were attached to the same CA atom of the backbone. Thus, the molecular topology follows the dual topology approach. The transformation was conducted in both the protein and aqueous environments. Each transformation (adding the proton to or removing it from Asp401) was carried out in three steps, as in our previous work.[74,75] In the first step, the partial charges of the side chain of pAsp401 were removed (i.e., the uncharging step). In the second step, the uncharged pAsp401 was transformed into an uncharged Asp401 with the soft-core potential (implemented by the PSSP routine in the PERT module).[76] In the final step, the partial charges on Asp401 were restored (i.e., the charging step). Because the third step brings a net charge, we varied the Na+ and Cl- numbers to eliminate the artifacts caused by the net charge during the transformation.[77]

Each transformation was accomplished in 11 λ intermediates (that is, λ = 0.0, 0.1, 0.2, 0.3, 0.4, 0.5, 0.6, 0.7, 0.8, 0.9, and 1.0 values), where λ is the coupling parameter for a linear transformation between the starting and end points. At each λ value, a total of 2 ns simulations were carried out, and the last 1 ns was used for the free energy calculations with the thermodynamic integration method (TI). To remove bias when estimating the free energy change, we extracted uncorrelated data by observing their correlation time. The bootstrapping protocol was applied to obtain precise average values of the free energies and their associated errors with 1000 repetitions for each transformation. The convergence of the final free energy value ($\Delta\Delta G$) was checked by plotting its time series (Figure S1). Although we conducted the transformation along one direction, i.e., from pAsp401 to Asp401, each transformation was started at λ = 0.5 (a middle point) and moved to the two opposite end points, i.e., λ = 0.0 and 1.0. In this way, the error caused by hysteresis was minimized. All simulations were carried out using the PERT module in the CHARMM program (version 42b2).

Metadynamics

One of the three tryptophans forming the m^{6}A cage adopts different conformations in its bound and unbound states. However, the conformational changes cannot be sampled sufficiently with unbiased MD simulations. To tackle this issue, metadynamics[40] was used to enhance the conformational changes. The metadynamics module implemented in NAMD (ver. 2.14) was used in this study.[64]

Trp497 of DF3 (Trp470 for DF1 and Trp491 for DF2) was the target for the enhanced sampling. Its orientation difference can be well represented by its dihedral angle χ_2 (CA-CB-CG-CD2 in Figure 3b). This dihedral angle was selected as the collective variable for the metadynamics simulations. The Gaussian "hill" was added to the original potential by setting the parameters "hillWeight" and "hillwidth" to 0.05 and 1.5, respectively. χ_2 ranged from −180 to 180° with a 2° bin width. The frequency of a newly added Gaussian hill was set to every 500 integration steps. A complete potential of mean force (PMF) profile was output every 10 ns. We conducted 5 replicas with 500 ns for each to ensure enough sampling and reproducibility. Here, we were only interested in the local conformational changes of the tryptophans, namely their flipping in the close binding pocket. Thus, the contribution from significant conformational changes, for example, the tryptophan flipping out of the binding pocket, was excluded. To map the final PMF profile (Figure 2c), we combined all PMF output files from 5 replicas, and the precise PMF values and their associated error were estimated by the bootstrapping method.

Gaussian Accelerated Molecular Dynamics (GaMD)

Gaussian accelerated MD (GaMD) simulations[41] were performed to observe significant conformational changes of Rec-loops of YTHDF1−3 starting from their close conformations. The system constructs are the same as in our previous work for consistency. GaMD was run with the dual boost potentials, and the threshold energy was set to its lower bound. The system was equilibrated for 10 ns by conventional MD simulations with backbone atoms restrained. Another 2 ns of conventional MD simulations were followed to collect the system potentials' upper and lower limits. The upper limit of the standard deviation of the total boost potential was set to 100 kcal/mol, and the upper limit of the standard deviation of the dihedral boost potential was assigned to 10 kcal/mol. These deviation limits allowed us to converge the force constant k_0 to 1.0 in 50 ns of equilibration GaMD simulations. Notably, we are here merely interested in observing events of large conformational changes but correctly reweighting the free energy landscapes for the changes, which allowed us to use large deviation limit values. The production GaMD simulations were conducted for one μs for each system without restraint on backbone atoms, and five replicas were produced with the same starting coordinates but different velocity vectors.

QM/MM MD Simulations

The CHARMM package[60] was employed for performing the present QM/MM simulations. In particular, the QM part was solved with the MNDO97 module.[78,79] The ligand 6MAP, i.e., m^{6}A, and the side chain of residue 401 (cut at Cα level) were included in the QM region. The generalized hybrid orbital (GHO) method[80] was used to cap covalent bonds at the QM/MM boundary. The total number of QM atoms was 43, with a resulting charge of −1. The QM region was modeled according to the AM1[81] set of parameters. The extended Lagrangian formulation with dissipation in the Born−Oppenheimer approximation[82,83] was used to boost the convergence of the self-consistent procedure. The initial path for our free energy calculations was obtained by gradually reducing the value of the reaction coordinate

$$\mu = r(\text{O-H}) - r(\text{N-H})\ (\text{Å})$$

while running 500 ABNR minimization steps. The proton was initially located on the m^{6}A side. This way, 39 windows were generated, spanning the range between −1 and 0.9 Å. An equilibration phase was performed, which consisted of 5 ns per window. Data production simulations were performed at 298.15 K in the constant pressure (CPT) ensemble with the Nosé−Hoover Langevin piston method.[65,66] The free energy profile was computed using the umbrella sampling (US) technique.[84] Three sets of simulations of 0.9, 0.6, and 0.3 ns per window were performed to compute error bars, resulting in 70.2 ns for the entire system.

Constant pH Simulations

The initial structures for the protein chains A and B in the dimer were taken from the structure 8BS4. The dimer structure was processed with the CHARMM-GUI tools[85] to add solvent water (33949 molecules) and Na (97 atoms) and Cl (140 atoms) ions in a cubic box of 105 Å in size. Parameters for particle interactions were taken from the CHARMM36

Downloaded from pubs.acs.org/jctcce/article-pdf/doi/10.1021/acs.jctc.6c01247/6884938/acs.jctc.6c01247.pdf by UNIV OF ZURICH user on 20 October 2026

https://doi.org/10.1021/acs.jctc.6c01247
J. Chem. Theory Comput. XXXX, XXX, XXX−XXX

force field. The initial protonation states of histidine residues were assigned based on their local hydrogen-bonding environments. Most histidines, including His538, were modeled in the neutral HSE tautomeric form. In contrast, His403 was assigned the doubly protonated, positively charged HSP state due to its direct interaction with the negatively charged side chain of Glu540. All glutamate and aspartate residues were modeled in their deprotonated (anionic) states, while all lysine residues were assigned their protonated (positively charged) forms. Cysteine residues were modeled in their neutral, thiol state. The particle mesh Ewald (PME) method was used to compute electrostatic interactions with a grid size of 1 Å and a sixth-order interpolation scheme. Bonds to hydrogens in the protein were kept rigid with the assistance of the ShakeH algorithm, and those in water molecules employed the SETTLE algorithm. An initial minimization step was done over 10,000 steps, where heavy atoms were harmonically restrained at their initial positions using a force constant of 1 kcal/mol/Å^2. This step was followed by an equilibration step in the NVT ensemble using a Langevin thermostat with a damping coefficient of 1/ps at a temperature of 303.15 K. This equilibration step was performed during 50 ns with a 2 fs time step.

The final structure from the equilibration step was employed as the initial structure for the constant pH MD (cpHMD) simulations implemented in NAMD v. 2.14. This method employs a hybrid nonequilibrium MD/Monte Carlo (neMD/MC) technique to sample protonation states of titratable residues.[86] All ASP, GLU, LYS, CYS, and HIS were considered as titratable residues during the simulations. pH values for the simulations were sampled in the range of 0.5 to 13.5 with a 0.5 unit separation, resulting in a total of 20 evenly spaced windows. Initially, 2.3 × 104 cycles comprising 500 MD steps and 7500 neMD/MC steps were done. Then, 2.76 × 104 cycles of 1000 MD steps and 7500 neMD/MC steps were conducted. The "cphanalyze" script from the PyNAMD package (https://github.com/radakb/pynamd/tree/master) was used to estimate the pK_a and Hill coefficient values with the Agresti-Coull method[87] from the results of all windows.

■ ASSOCIATED CONTENT

Data Availability Statement

The 3D coordinates of the prepared systems used for the MD simulations are provided in the Supporting Information and are described and listed in Table S2.

Supporting Information

The Supporting Information is available free of charge at https://pubs.acs.org/doi/10.1021/acs.jctc.6c01247.

Archive of 3D coordinates of prepared systems for MD simulations reported in the article (ZIP)

Experimental and simulation methods; X-ray crystallographic statistical data; ITC titration curves; and more figures for the analyses of MD simulations (PDF)

Accession Codes

The atomic coordinates and structure factors for the three crystal structures have been deposited in the Protein Data Bank (PDB) with the accession codes 8BS4, 8BS5, and 8BS6.

■ AUTHOR INFORMATION

Corresponding Author

Amedeo Caflisch − *Department of Biochemistry, University of Zurich, CH-8057 Zurich, Switzerland;* orcid.org/0000-0002-2317-6792; Phone: +41 44 635 5521; Email: caflisch@bioc.uzh.ch

Authors

Yaozong Li − *Department of Biochemistry, University of Zurich, CH-8057 Zurich, Switzerland; Department of Chemistry, Umeå University, SE-901 87 Umeå, Sweden;* orcid.org/0000-0002-5796-2644

Rajiv Kumar Bedi − *Department of Biochemistry, University of Zurich, CH-8057 Zurich, Switzerland;* orcid.org/0000-0002-8193-9006

Pedro Ojeda-May − *High Performance Computing Center North (HPC2N), Umeå University, SE-901 87 Umeå, Sweden*

Complete contact information is available at: https://pubs.acs.org/10.1021/acs.jctc.6c01247

Author Contributions

‖Y.L. and R.K.B. contributed equally to this work. Y.L., R.K.B., and A.C. conceived the original ideas and designed the experiments. R.K.B. carried out wet lab experiments. Y.L. conducted most molecular dynamics simulations and wrote the first draft. P.O.M. performed the QM/MM and cpHMD simulations. All authors critically revised and improved the manuscript. A.C. supervised the project.

Funding

This work was supported by the International Postdoc Grant funded by the Swedish Research Council (Grant VR 2019−00608 to Y.L.) and the Swiss National Science Foundation (310030−212195 to A.C.).

Notes

The authors declare no competing financial interest.

■ ACKNOWLEDGMENTS

We thank Beat Blattmann at the Protein Crystallization Center (University of Zurich) for assistance with crystallization screening. The use of beamlines and user support at the Swiss Light Source is gratefully acknowledged. The authors thank the Swiss National Supercomputing Centre (CSCS) in Lugano and the Swedish National Infrastructure for Computing (SNIC) at the High-Performance Computing Center North (HPC2N) for providing the computational resources. The authors thank Dr. Xiang Wang for useful discussions. Y.L. thanks Dr. Lars Wiedmer for his support when the work was initiated.

■ REFERENCES

(1) He, C. Grand challenge commentary: RNA epigenetics? *Nat. Chem. Biol.* **2010**, *6* (12), 863−865.

(2) Meyer, K. D.; Saletore, Y.; Zumbo, P.; Elemento, O.; Mason, C. E.; Jaffrey, S. R. Comprehensive Analysis of mRNA Methylation Reveals Enrichment in 3 ' UTRs and near Stop Codons. *Cell* **2012**, *149* (7), 1635−1646.

(3) Roundtree, I. A.; Evans, M. E.; Pan, T.; He, C. Dynamic RNA Modifications in Gene Expression Regulation. *Cell* **2017**, *169* (7), 1187−1200.

(4) Wang, Y.; Li, Y.; Toth, J. I.; Petroski, M. D.; Zhang, Z. L.; Zhao, J. C. N-6-methyladenosine modification destabilizes developmental

Downloaded from pubs.acs.org/jctcce/article-pdf/doi/10.1021/acs.jctc.6c01247/6884938/acs.jctc.6c01247.pdf by UNIV OF ZURICH user on 20 October 2026

regulators in embryonic stem cells. *Nat. Cell Biol.* **2014**, *16* (2), 191−198.
(5) Jia, G. F.; Fu, Y.; Zhao, X.; Dai, Q.; Zheng, G. Q.; Yang, Y.; Yi, C. Q.; Lindahl, T.; Pan, T.; Yang, Y. G.; He, C. N6-Methyladenosine in nuclear RNA is a major substrate of the obesity-associated FTO. *Nat. Chem. Biol.* **2011**, *7* (12), 885−887.
(6) Zheng, G. Q.; Dahl, J. A.; Niu, Y. M.; Fedorcsak, P.; Huang, C. M.; Li, C. J.; Vagbo, C. B.; Shi, Y.; Wang, W. L.; Song, S. H.; et al. ALKBH5 Is a Mammalian RNA Demethylase that Impacts RNA Metabolism and Mouse Fertility. *Mol. Cell* **2013**, *49* (1), 18−29.
(7) Dominissini, D.; Moshitch-Moshkovitz, S.; Schwartz, S.; Salmon-Divon, M.; Ungar, L.; Osenberg, S.; Cesarkas, K.; Jacob-Hirsch, J.; Amariglio, N.; Kupiec, M.; et al. Topology of the human and mouse m(6)A RNA methylomes revealed by m(6)A-seq. *Nature* **2012**, *485* (7397), U201−U284.
(8) Hsu, P. J.; Zhu, Y. F.; Ma, H. H.; Guo, Y. H.; Shi, X. D.; Liu, Y. Y.; Qi, M. J.; Lu, Z. K.; Shi, H. L.; Wang, J. Y.; et al. Ythdc2 is an N-6-methyladenosine binding protein that regulates mammalian spermatogenesis. *Cell Res.* **2017**, *27* (9), 1115−1127.
(9) Wang, X.; Lu, Z. K.; Gomez, A.; Hon, G. C.; Yue, Y. N.; Han, D. L.; Fu, Y.; Parisien, M.; Dai, Q.; Jia, G. F.; et al. N-6-methyladenosine-dependent regulation of messenger RNA stability. *Nature* **2014**, *505* (7481), 117−120.
(10) Huang, H.; Weng, H.; Sun, W.; Qin, X.; Shi, H.; Wu, H.; Zhao, B. S.; Mesquita, A.; Liu, C.; Yuan, C. L.; et al. Recognition of RNA N(6)-methyladenosine by IGF2BP proteins enhances mRNA stability and translation. *Nat. Cell Biol.* **2018**, *20* (3), 285−295.
(11) Wang, X.; Zhao, B. S.; Roundtree, I. A.; Lu, Z. K.; Han, D. L.; Ma, H. H.; Weng, X. C.; Chen, K.; Shi, H. L.; He, C. N-6-methyladenosine Modulates Messenger RNA Translation Efficiency. *Cell* **2015**, *161* (6), 1388−1399.
(12) Du, H.; Zhao, Y.; He, J.; Zhang, Y.; Xi, H.; Liu, M.; Ma, J.; Wu, L. YTHDF2 destabilizes m(6)A-containing RNA through direct recruitment of the CCR4-NOT deadenylase complex. *Nat. Commun.* **2016**, *7*, No. 12626.
(13) Shi, H.; Wang, X.; Lu, Z.; Zhao, B. S.; Ma, H.; Hsu, P. J.; Liu, C.; He, C. YTHDF3 facilitates translation and decay of N(6)-methyladenosine-modified RNA. *Cell Res.* **2017**, *27* (3), 315−328.
(14) Zaccara, S.; Jaffrey, S. R. A Unified Model for the Function of YTHDF Proteins in Regulating m(6)A-Modified mRNA. *Cell* **2020**, *181* (7), 1582−1595.e18.
(15) Nai, F.; Nachawati, R.; Zalesak, F.; Wang, X.; Li, Y.; Caflisch, A. Fragment Ligands of the m(6)A-RNA Reader YTHDF2. *ACS Med. Chem. Lett.* **2022**, *13* (9), 1500−1509.
(16) Li, Y.; Bedi, R. K.; Moroz-Omori, E. V.; Caflisch, A. Structural and Dynamic Insights into Redundant Function of YTHDF Proteins. *J. Chem. Inf. Model.* **2020**, *60*, 5932.
(17) Xu, C.; Liu, K.; Ahmed, H.; Loppnau, P.; Schapira, M.; Min, J. R. Structural Basis for the Discriminative Recognition of N-6-Methyladenosine RNA by the Human YT521-B Homology Domain Family of Proteins. *J. Biol. Chem.* **2015**, *290* (41), 24902−24913.
(18) Wiedmer, L.; Eberle, S. A.; Bedi, R. K.; Sledz, P.; Caflisch, A. A Reader-Based Assay for m(6)A Writers and Erasers. *Anal. Chem.* **2019**, *91* (4), 3078−3084.
(19) Wang, J.; Wang, L.; Diao, J.; Shi, Y. G.; Shi, Y.; Ma, H.; Shen, H. Binding to m(6)A RNA promotes YTHDF2-mediated phase separation. *Protein Cell* **2020**, *11* (4), 304−307.
(20) Ries, R. J.; Zaccara, S.; Klein, P.; Olarerin-George, A.; Namkoong, S.; Pickering, B. F.; Patil, D. P.; Kwak, H.; Lee, J. H.; Jaffrey, S. R. m(6)A enhances the phase separation potential of mRNA. *Nature* **2019**, *571* (7765), 424−428.
(21) Gao, Y.; Pei, G.; Li, D.; Li, R.; Shao, Y.; Zhang, Q. C.; Li, P. Multivalent m(6)A motifs promote phase separation of YTHDF proteins. *Cell Res.* **2019**, *29* (9), 767−769.
(22) Dixit, D.; Prager, B. C.; Gimple, R. C.; Poh, H. X.; Wang, Y.; Wu, Q.; Qiu, Z.; Kidwell, R. L.; Kim, L. J. Y.; Xie, Q.; et al. The RNA m6A Reader YTHDF2Maintains Oncogene Expression and Is a Targetable Dependency in Glioblastoma Stem Cells. *Cancer Discovery* **2021**, *11* (2), 480−499.
(23) Sheng, H.; Li, Z.; Su, S.; Sun, W.; Zhang, X.; Li, L.; Li, J.; Liu, S.; Lu, B.; Zhang, S.; Shan, C. YTH domain family 2 promotes lung cancer cell growth by facilitating 6-phosphogluconate dehydrogenase mRNA translation. *Carcinogenesis* **2020**, *41* (5), 541−550.
(24) Liu, T.; Wei, Q.; Jin, J.; Luo, Q.; Liu, Y.; Yang, Y.; Cheng, C.; Li, L.; Pi, J.; Si, Y.; et al. The m6A reader YTHDF1 promotes ovarian cancer progression via augmenting EIF3C translation. *Nucleic Acids Res.* **2020**, *48* (7), 3816−3831.
(25) Li, J.; Xie, H.; Ying, Y.; Chen, H.; Yan, H.; He, L.; Xu, M.; Xu, X.; Liang, Z.; Liu, B.; et al. YTHDF2 mediates the mRNA degradation of the tumor suppressors to induce AKT phosphorylation in N6-methyladenosine-dependent way in prostate cancer. *Mol. Cancer* **2020**, *19* (1), 152.
(26) Paris, J.; Morgan, M.; Campos, J.; Spencer, G. J.; Shmakova, A.; Ivanova, I.; Mapperley, C.; Lawson, H.; Wotherspoon, D. A.; Sepulveda, C.; et al. Targeting the RNA m(6)A Reader YTHDF2 Selectively Compromises Cancer Stem Cells in Acute Myeloid Leukemia. *Cell Stem Cell* **2019**, *25* (1), 137−148 e136.
(27) Ni, W.; Yao, S.; Zhou, Y.; Liu, Y.; Huang, P.; Zhou, A.; Liu, J.; Che, L.; Li, J. Long noncoding RNA GAS5 inhibits progression of colorectal cancer by interacting with and triggering YAP phosphorylation and degradation and is negatively regulated by the m(6)A reader YTHDF3. *Mol. Cancer* **2019**, *18* (1), 143.
(28) Jia, R.; Chai, P.; Wang, S.; Sun, B.; Xu, Y.; Yang, Y.; Ge, S.; Jia, R.; Yang, Y. G.; Fan, X. m(6)A modification suppresses ocular melanoma through modulating HINT2 mRNA translation. *Mol. Cancer* **2019**, *18* (1), 161.
(29) Hou, J.; Zhang, H.; Liu, J.; Zhao, Z.; Wang, J.; Lu, Z.; Hu, B.; Zhou, J.; Zhao, Z.; Feng, M.; et al. YTHDF2 reduction fuels inflammation and vascular abnormalization in hepatocellular carcinoma. *Mol. Cancer* **2019**, *18* (1), 163.
(30) Zou, Z.; Sepich-Poore, C.; Zhou, X.; Wei, J.; He, C. The mechanism underlying redundant functions of the YTHDF proteins. *Genome Biol.* **2023**, *24* (1), 17.
(31) Li, Y.; Bedi, R. K.; Nai, F.; Roten, V.; Dolbois, A.; Záleš̆ák, F.; Nachawati, R.; Huang, D.; Caflisch, A. Structure-based design of ligands of the m6A-RNA reader YTHDC1. *European J. Med. Chem. Rep.* **2022**, *5*, No. 100057.
(32) Li, Y.; Bedi, R. K.; Wiedmer, L.; Sun, X.; Huang, D.; Caflisch, A. Atomistic and Thermodynamic Analysis of N6-Methyladenosine (m(6)A) Recognition by the Reader Domain of YTHDC1. *J. Chem. Theory Comput.* **2021**, *17*, 1240.
(33) Bedi, R. K.; Huang, D.; Wiedmer, L.; Li, Y.; Dolbois, A.; Wojdyla, J. A.; Sharpe, M. E.; Caflisch, A.; Sledz, P. Selectively Disrupting m(6)A-Dependent Protein-RNA Interactions with Fragments. *ACS Chem. Biol.* **2020**, *15* (3), 618−625.
(34) Li, Y. Z.; Bedi, R. K.; Wiedmer, L.; Huang, D. Z.; Sledz, P.; Caflisch, A. Flexible Binding of m(6)A Reader Protein YTHDC1 to Its Preferred RNA Motif. *J. Chem. Theory Comput.* **2019**, *15* (12), 7004−7014.
(35) Widmer, J.; Vitalis, A.; Caflisch, A. On the specificity of the recognition of m6A-RNA by YTH reader domains. *J. Biol. Chem.* **2024**, *300* (12), 107998.
(36) Bedi, R. K.; Caflisch, A. A. DNA-Based Binding Assay for the m A-RNA Reader Proteins. *ChemBioChem* **2026**, *27* (6), e202500897 DOI: 10.1002/cbic.202500897.
(37) Kampf, G.; Kapinos, L. E.; Griesser, R.; Lippert, B.; Sigel, H. Comparison of the acid-base properties of purine derivatives in aqueous solution. Determination of intrinsic proton affinities of various basic sites. *J. Chem. Society-Perkin Transactions 2* **2002**, No. 7, 1320−1327.
(38) Field, M. J.; Bash, P. A.; Karplus, M. A Combined Quantum-Mechanical and Molecular Mechanical Potential for Molecular-Dynamics Simulations. *J. Comput. Chem.* **1990**, *11* (6), 700−733.
(39) MarvinSketch 21.20.0, ChemAxon (http://www.chemaxon.com).
(40) Laio, A.; Parrinello, M. Escaping free-energy minima. *Proc. Natl. Acad. Sci. U.S.A.* **2002**, *99* (20), 12562−12566.

Downloaded from pubs.acs.org/jctcce/article-pdf/doi/10.1021/acs.jctc.6c01247/6884938/acs.jctc.6c01247.pdf by UNIV OF ZURICH user on 20 October 2026

(41) Miao, Y. L.; Feher, V. A.; McCammon, J. A. Gaussian Accelerated Molecular Dynamics: Unconstrained Enhanced Sampling and Free Energy Calculation. *J. Chem. Theory Comput.* **2015**, *11* (8), 3584−3595.
(42) Alberti, S.; Gladfelter, A.; Mittag, T. Considerations and Challenges in Studying Liquid-Liquid Phase Separation and Biomolecular Condensates. *Cell* **2019**, *176* (3), 419−434.
(43) Vondrášek, J.; Mason, P. E.; Heyda, J.; Collins, K. D.; Jungwirth, P. The Molecular Origin of Like-Charge Arginine-Arginine Pairing in Water. *J. Phys. Chem. B* **2009**, *113* (27), 9041−9045.
(44) Martins de Oliveira, V.; Liu, R.; Shen, J. Constant pH molecular dynamics simulations: Current status and recent applications. *Curr. Opin Struct. Biol.* **2022**, *77*, No. 102498.
(45) Henderson, J. A.; Shen, J. Exploring the pH- and Ligand-Dependent Flap Dynamics of Malarial Plasmepsin II. *J. Chem. Inf. Model* **2022**, *62* (1), 150−158.
(46) Henderson, J. A.; Liu, R.; Harris, J. A.; Huang, Y.; de Oliveira, V. M.; Shen, J. A Guide to the Continuous Constant pH Molecular Dynamics Methods in Amber and CHARMM [Article v1.0]. *Living J. Comput. Mol. Sci.* **2022**, *4* (1), 1563 DOI: 10.33011/livecoms.4.1.1563.
(47) Harris, J. A.; Liu, R.; Martins de Oliveira, V.; Vazquez-Montelongo, E. A.; Henderson, J. A.; Shen, J. GPU-Accelerated All-Atom Particle-Mesh Ewald Continuous Constant pH Molecular Dynamics in Amber. *J. Chem. Theory Comput.* **2022**, *18* (12), 7510−7527.
(48) Ellis, C. R.; Shen, J. pH-Dependent Population Shift Regulates BACE1 Activity and Inhibition. *J. Am. Chem. Soc.* **2015**, *137* (30), 9543−9546.
(49) Turner, L. D.; Trinh, C. H.; Hubball, R. A.; Orritt, K. M.; Lin, C. C.; Burns, J. E.; Knowles, M. A.; Fishwick, C. W. G. From Fragment to Lead: De Novo Design and Development toward a Selective FGFR2 Inhibitor. *J. Med. Chem.* **2022**, *65* (2), 1481−1504.
(50) Invernizzi, A.; Nai, F.; Bedi, R. K.; Vargas-Rosales, P. A.; Li, Y.; Bochenkova, E.; Herok, M.; Zalesak, F.; Caflisch, A. Discovery of YTHDF2 Ligands by Fragment-Based Design. *ACS Bio Med. Chem. Au* **2025**, *5* (4), 753−765.
(51) Casey, J. R.; Grinstein, S.; Orlowski, J. Sensors and regulators of intracellular pH. *Nat. Rev. Mol. Cell Biol.* **2010**, *11* (1), 50−61.
(52) Persi, E.; Duran-Frigola, M.; Damaghi, M.; Roush, W. R.; Aloy, P.; Cleveland, J. L.; Gillies, R. J.; Ruppin, E. Systems analysis of intracellular pH vulnerabilities for cancer therapy. *Nat. Commun.* **2018**, *9*, No. 57, DOI: 10.1038/s41467-018-05261-x.
(53) Fu, Y.; Zhuang, X. m(6)A-binding YTHDF proteins promote stress granule formation. *Nat. Chem. Biol.* **2020**, *16* (9), 955−963.
(54) Lin, H. J.; Herman, P.; Lakowicz, J. R. Fluorescence lifetime-resolved pH imaging of living cells. *Cytometry A* **2003**, *52A* (2), 77−89.
(55) Le Guilloux, V.; Schmidtke, P.; Tuffery, P. Fpocket: an open source platform for ligand pocket detection. *BMC Bioinf.* **2009**, *10*, 168.
(56) Micaelli, M.; Dalle Vedove, A.; Cerofolini, L.; Vigna, J.; Sighel, D.; Zaccara, S.; Bonomo, I.; Poulentzas, G.; Rosatti, E. F.; Cazzanelli, G.; et al. Small-Molecule Ebselen Binds to YTHDF Proteins Interfering with the Recognition of N (6)-Methyladenosine-Modified RNAs. *ACS Pharmacol. Transl. Sci.* **2022**, *5* (10), 872−891.
(57) Hao, W.; Dian, M.; Zhou, Y.; Zhong, Q.; Pang, W.; Li, Z.; Zhao, Y.; Ma, J.; Lin, X.; Luo, R.; et al. Autophagy induction promoted by m(6)A reader YTHDF3 through translation upregulation of FOXO3 mRNA. *Nat. Commun.* **2022**, *13* (1), No. 5845.
(58) Lasman, L.; Krupalnik, V.; Viukov, S.; Mor, N.; Aguilera-Castrejon, A.; Schneir, D.; Bayerl, J.; Mizrahi, O.; Peles, S.; Tawil, S.; et al. Context-dependent functional compensation between Ythdf m A reader proteins. *Gene Dev.* **2020**, *34* (19−20), 1373−1391.
(59) Kontur, C.; Jeong, M.; Cifuentes, D.; Giraldez, A. J. Ythdf m(6)A Readers Function Redundantly during Zebrafish Development. *Cell Rep.* **2020**, *33* (13), No. 108598.
(60) Brooks, B. R.; Brooks, C. L.; Mackerell, A. D.; Nilsson, L.; Petrella, R. J.; Roux, B.; Won, Y.; Archontis, G.; Bartels, C.; Boresch, S.; et al. CHARMM: The Biomolecular Simulation Program. *J. Comput. Chem.* **2009**, *30* (10), 1545−1614.
(61) Jorgensen, W. L.; Chandrasekhar, J.; Madura, J. D.; Impey, R. W.; Klein, M. L. Comparison of Simple Potential Functions for Simulating Liquid Water. *J. Chem. Phys.* **1983**, *79* (2), 926−935.
(62) Waterhouse, A.; Bertoni, M.; Bienert, S.; Studer, G.; Tauriello, G.; Gumienny, R.; Heer, F. T.; de Beer, T. A. P.; Rempfer, C.; Bordoli, L.; et al. SWISS-MODEL: homology modelling of protein structures and complexes. *Nucleic Acids Res.* **2018**, *46* (W1), W296−W303.
(63) Šali, A.; Blundell, T. L. Comparative protein modelling by satisfaction of spatial restraints. *J. Mol. Biol.* **1993**, *234* (3), 779−815.
(64) Phillips, J. C.; Braun, R.; Wang, W.; Gumbart, J.; Tajkhorshid, E.; Villa, E.; Chipot, C.; Skeel, R. D.; Kale, L.; Schulten, K. Scalable molecular dynamics with NAMD. *J. Comput. Chem.* **2005**, *26* (16), 1781−1802.
(65) Martyna, G. J.; Tobias, D. J.; Klein, M. L. Constant-Pressure Molecular-Dynamics Algorithms. *J. Chem. Phys.* **1994**, *101* (5), 4177−4189.
(66) Feller, S. E.; Zhang, Y. H.; Pastor, R. W.; Brooks, B. R. Constant-Pressure Molecular-Dynamics Simulation - the Langevin Piston Method. *J. Chem. Phys.* **1995**, *103* (11), 4613−4621.
(67) Steinbach, P. J.; Brooks, B. R. New Spherical-Cutoff Methods for Long-Range Forces in Macromolecular Simulation. *J. Comput. Chem.* **1994**, *15* (7), 667−683.
(68) Essmann, U.; Perera, L.; Berkowitz, M. L.; Darden, T.; Lee, H.; Pedersen, L. G. A Smooth Particle Mesh Ewald Method. *J. Chem. Phys.* **1995**, *103* (19), 8577−8593.
(69) Shirts, M. R.; Mobley, D. L.; Chodera, J. D.; Pande, V. S. Accurate and efficient corrections for missing dispersion interactions in molecular Simulations. *J. Phys. Chem. B* **2007**, *111* (45), 13052−13063.
(70) Huang, J.; MacKerell, A. D. CHARMM36 all-atom additive protein force field: Validation based on comparison to NMR data. *J. Comput. Chem.* **2013**, *34* (25), 2135−2145.
(71) MATLAB 2018a, T. M. W., Inc.
(72) The PyMOL Molecular Graphics System, V. S., LLC.
(73) Maestro 11.5, S., LLC, New York, NY, 2018.
(74) Li, Y.; Nam, K. Repulsive Soft-Core Potentials for Efficient Alchemical Free Energy Calculations. *J. Chem. Theory Comput.* **2020**, *16* (8), 4776−4789.
(75) Li, Y. Z.; Nam, K. Dynamic, structural and thermodynamic basis of insulin-like growth factor 1 kinase allostery mediated by activation loop phosphorylation. *Chem. Sci.* **2017**, *8* (5), 3453−3464.
(76) Zacharias, M.; Straatsma, T. P.; Mccammon, J. A. Separation-Shifted Scaling, a New Scaling Method for Lennard-Jones Interactions in Thermodynamic Integration. *J. Chem. Phys.* **1994**, *100* (12), 9025−9031.
(77) Morgan, B. R.; Massi, F. Accurate Estimates of Free Energy Changes in Charge Mutations. *J. Chem. Theory Comput.* **2010**, *6* (6), 1884−1893.
(78) Nam, K. Acceleration of Ab Initio QM/MM Calculations under Periodic Boundary Conditions by Multiscale and Multiple Time Step Approaches. *J. Chem. Theory Comput.* **2014**, *10* (10), 4175−4183.
(79) Nam, K.; Gao, J.; York, D. M. An Efficient Linear-Scaling Ewald Method for Long-Range Electrostatic Interactions in Combined QM/MM Calculations. *J. Chem. Theory Comput.* **2005**, *1* (1), 2−13.
(80) Gao, J. L.; Amara, P.; Alhambra, C.; Field, M. J. A generalized hybrid orbital (GHO) method for the treatment of boundary atoms in combined QM/MM calculations. *J. Phys. Chem. A* **1998**, *102* (24), 4714−4721.
(81) Dewar, M. J. S.; Zoebisch, E. G.; Healy, E. F.; Stewart, J. J. P. The Development and Use of Quantum-Mechanical Molecular-Models. 76. Am1 - a New General-Purpose Quantum-Mechanical Molecular-Model. *J. Am. Chem. Soc.* **1985**, *107* (13), 3902−3909.
(82) Zheng, G. S.; Niklasson, A. M. N.; Karplus, M. Lagrangian formulation with dissipation of Born-Oppenheimer molecular dynamics using the density-functional tight-binding method. *J. Chem. Phys.* **2011**, *135* (4), R1297 DOI: 10.1063/1.3605303.

Downloaded from pubs.acs.org/jctcce/article-pdf/doi/10.1021/acs.jctc.6c01247/6884938/acs.jctc.6c01247.pdf by UNIV OF ZURICH user on 20 October 2026

(83) Niklasson, A. M. N.; Steneteg, P.; Odell, A.; Bock, N.; Challacombe, M.; Tymczak, C. J.; Holmstrom, E.; Zheng, G.; Weber, V. Extended Lagrangian Born-Oppenheimer molecular dynamics with dissipation. *J. Chem. Phys.* **2009**, *130* (21), No. 214109.
(84) Torrie, G. M.; Valleau, J. P. Non-Physical Sampling Distributions in Monte-Carlo Free-Energy Estimation - Umbrella Sampling. *J. Comput. Phys.* **1977**, *23* (2), 187−199.
(85) Jo, S.; Kim, T.; Iyer, V. G.; Im, W. CHARMM-GUI: a web-based graphical user interface for CHARMM. *J. Comput. Chem.* **2008**, *29* (11), 1859−1865.
(86) Radak, B. K.; Chipot, C.; Suh, D.; Jo, S.; Jiang, W.; Phillips, J. C.; Schulten, K.; Roux, B. Constant-pH Molecular Dynamics Simulations for Large Biomolecular Systems. *J. Chem. Theory Comput.* **2017**, *13* (12), 5933−5944.
(87) Agresti, A.; Coull, B. A. Approximate is better than "exact" for interval estimation of binomial proportions. *Am. Stat.* **1998**, *52* (2), 119−126.

Downloaded from pubs.acs.org/jctcce/article-pdf/doi/10.1021/acs.jctc.6c01247/6884938/acs.jctc.6c01247.pdf by UNIV OF ZURICH user on 20 October 2026

https://doi.org/10.1021/acs.jctc.6c01247
J. Chem. Theory Comput. XXXX, XXX, XXX−XXX